Politecnico di Torino

Department of Environment,
Land and Infrastructure Engineering

Master's Degree in Civil Engineering

Effect of Aggregate Angularity and Binder Ratio on the Compaction and Strength Properties of Porous Concrete: An Investigation into Self-Compacting Design

Supervisors:
Prof. Marco Bassani
Prof. Luca Tefa

Candidate:
Arash Fakhournezhad

July 2026

Abstract

Pervious pavements made up of porous concrete are increasingly utilised as a climate adaptation tool to manage stormwater runoff, replenish groundwater, and mitigate urban heat island effects. However, the widespread use of porous concrete is often limited by its stiff, low-slump consistency, which also hinders uniform field placement. Moreover, the absence of standardised workability criteria leaves the quality of compaction dependent on subjective judgment. While slipform paving offers a suitable method for mechanised, consistent placement, the substantial compaction energy it delivers exceeds the conditions under which existing workability frameworks were developed. The combined effect of aggregate angularity and paste volume on the compaction and strength properties of porous concrete under heavy mechanised placement has not previously been quantified in a volumetrically controlled framework. Quantifying this combined effect is essential to establishing design criteria for self-compacting porous concrete mixtures that enable uniform mechanised placement.

This research investigates the interactive effects of coarse aggregate angularity and the binder-to-aggregate (b/a) mass ratio on the fresh-state compaction indices and the tensile strength of porous concrete, conducted under the PORO-CITY project. A laboratory experimental investigation was designed and conducted to evaluate the effect of the three aggregate morphologies — 100% rounded river gravel, 100% crushed aggregate, and a 50/50 blend — each at ratios of 18%, 21%, and 24%. All aggregates were sourced from the same quarry to eliminate mineralogical variability. A Superpave Gyratory Compactor was operated at 200 kPa using a constant-volume “stop-at-height” protocol that fixed the design void content at 20% across all specimens. Fresh-state compaction indices were characterised through the workability energy index (WEI) and compaction densification index (CDI). Mechanical performance was evaluated using 7-day indirect tensile strength, measured in three replicates. Mixture design porosity was verified using the water displacement procedure established by Montes et al. (2005), which is based on Archimedes' principle.

The results demonstrate that mixtures comprising 100% rounded aggregates achieve high initial flowability and require minimal compaction effort. However, this workability is inversely related to mechanical performance due to the limited interlock among mechanically aggregated rounded particles. At the other end, 100% crushed aggregate mixtures develop high tensile strength, but their high internal friction impedes compaction to the point that field placement becomes difficult, especially at low paste volumes. The 50/50 blended mixtures resolve this conflict. Their fresh-state behaviour is similar to that of the rounded particles, while the retained crushed fraction preserves the interlock needed to maintain structural performance. The 50/50 blend at 24% emerges as the optimal design in the experimental matrix to achieve self-compaction behaviour without compromising mechanical performance.

Keywords: Porous Concrete, Aggregate Angularity, Self-compacting Porous Concrete, Pervious Road Pavement, Superpave Gyratory Compactor, Compaction Indices.

Table of Contents

1. Introduction

1.1 Background and Motivation

Rapid urbanisation has altered natural hydrological cycles by replacing permeable soils with impervious surfaces such as conventional asphalt and concrete pavements. This transformation reduces natural water infiltration, increasing stormwater runoff, flood risk, and the transport of urban pollutants into aquatic ecosystems. In response, modern infrastructure engineering has increasingly adopted Green Infrastructure and Low Impact Development strategies.

Among these strategies, Portland Cement Porous Concrete (PCPC) has emerged as an effective sustainable pervious pavement material. PCPC is designed with a matrix of interconnected voids, typically around 20% to 25% porosity, which allows rainwater to pass directly through the pavement surface and into underlying storage layers or natural subgrades. This is achieved by carefully balancing aggregate gradation and cementitious paste volume, generally by eliminating or reducing the fine aggregate fraction. Beyond stormwater management, PCPC also reduces the urban heat island effect and lowers tire-pavement interaction noise.

Despite these environmental advantages, widespread field implementation of PCPC remains constrained by distinct engineering limitations categorised into fresh-state rheological anomalies and cured-state mechanical vulnerabilities (Kevern et al., 2009; Chandrappa and Biligiri, 2016). In its fresh state, the material's stiff, low-slump consistency makes conventional slump testing ineffective, causing field quality control to rely on subjective visual assessments—such as checking the plastic mixture's qualitative ability to form a cohesive ball by hand as seen in Figure 1.1—rather than utilising quantifiable, performance-based workability criteria (Tennis et al., 2004; Kevern et al., 2009).

Figure 1.1: Subjective visual assessment of fresh porous concrete workability using the qualitative manual hand-ball test under varying water contents (adapted from Tennis et al., 2004)

This lack of standardisation makes a labour-intensive placement workflow (Figure 1.2), requiring extensive manual raking and mechanical compaction via weighted steel rollers or roller-screeds to force the open-graded skeleton into its design density (Kevern et al., 2009). Furthermore, the material is inherently limited in its cured state; specifically, the structural requirement to maintain an interconnected macro-pore network to manage stormwater runoff creates a direct inverse relationship between void content and load-carrying capacity, restricting characteristic compressive strengths to a modest range of 2.8 to 28 MPa (ACI 522 Committee, 2006).

Figure 1.2: Field demonstration of the porous concrete placement workflow (adapted from Nassiri et al., 2017)

As established by Kevern et al. (2009), the manual compaction approach can produce density and compaction non-uniformity across the pavement section. Areas directly beneath the discharge point receive disproportionately high compaction, while adjacent raked areas remain under-compacted. This inconsistency generates localised structural weaknesses, uneven surface porosity, and variable tire-pavement interaction noise, which in turn accelerates surface raveling and degrades long-term durability.

This research is carried out under the framework of the PORO-CITY project, whose primary objective is to develop self-compacting porous concrete (SCPC) mixtures with controlled porosity. A mixture that flows and self-arranges without external compaction can guarantee uniform mechanical, thermophysical, and environmental performance across the full slab area. Bypassing manual compaction also streamlines the construction workflow, reducing operational costs, installation time, and construction-phase environmental impacts.

Achieving a true self-compacting state requires a delicate and meticulous control of the mix design variables. The extensive work carried out by Kevern et al. (2009) on fresh-state parameters demonstrated that factors such as the water-to-cement (w/c) ratio, chemical admixture schemes, sand additions, and mixing times each exert distinct influence over placement. His framework established that the binder-to-aggregate (b/a) mass ratio governs a mixture's internal workability and compaction indices far more than adjustments to water content alone. However, the research explicitly identified the effect of aggregate angularity on porous concrete placement and self-compaction as an unresolved variable. Because the coarse aggregate forms the primary structural skeleton of porous concrete, the surface texture and particle morphology of angular particles alter paste demand and compaction resistance in ways that have not been systematically quantified.

The primary goal of this thesis is to address this gap. By systematically evaluating the combined effects of coarse aggregate angularity and b/a ratio under high-energy compaction conditions, the research aims to identify the physical and rheological thresholds required to achieve a high-performance, self-compacting porous concrete for pervious road pavements.

1.2 Problem Statement

A major barrier to the standardisation of porous concrete is the inconsistency between laboratory-developed mixtures and field performance. Historically, fresh-state consistency has been treated more as an "art form" than a quantifiable property, relying on subjective assessments such as the contractor's ability to shape with hands a small quantity of plastic mixture into a cohesive ball (Tennis et al., 2004). Since conventional slump tests are largely ineffective for these stiff, low-slump mixtures, a standardised, performance-based workability method is needed to support large-scale infrastructure deployment.

When PCPC mixtures that perform well in the laboratory stiffen during transport, field operators frequently resort to adding water on-site to recover workability. This practice disrupts the engineered w/c ratio, reducing paste viscosity and causing the paste to drain downward. The result is permanent clogging of the lower water-carrying pores, alongside reduced mechanical strength and degraded freeze-thaw durability (Kevern et al., 2009).

While Kevern et al. (2009) have demonstrated that porous concrete workability can be characterised using a Superpave Gyratory Compactor (SGC), three important limitations remain.

First, standard asphalt-industry SGC units operate under high vertical compaction pressures — typically 600 kPa as required by the Asphalt Institute (AI, 2001) for hot-mix asphalt. To adapt this equipment for porous concrete, Kevern et al. (2009) modified a standard unit by removing its high-pressure hydraulic orifice, reducing the vertical pressure to 60 kPa to replicate the minimal energy of manual hand-rollers and lightweight screeds, which exert between 2.9 kPa and 40.0 kPa on the pavement surface, depending on roller type and pass number (Kevern, 2008). However, modern porous concrete is increasingly placed using slipform pavers, which deliver higher compaction energy than manual rollers through internal vibration and weighted strike-off screeds. The 60 kPa baseline is therefore unrepresentative of current mechanised placement conditions.

Second, since the compaction energy of slipform pavers exceeds that of manual hand-rollers, and since 200 kPa represents the minimum pressure achievable on an unmodified laboratory SGC without device-specific modification (Kevern et al., 2009), this study adopts 200 kPa as a base simulation for mechanised placement. Beyond its representativeness of field conditions, this pressure level has an additional practical advantage: it serves as a standardised, reproducible testing condition that requires no machine modification, no specialised calibration, and no device-specific adjustments (Figure 1.3). Any laboratory equipped with a standard SGC unit can replicate this compaction condition directly, making the methodology transferable and consistent across research programs without the constraints caused by modifying low-pressure setup.

Figure 1.3: The standard Superpave Gyratory Compactor equipment and integrated data-acquisition system used to characterise fresh-state porous concrete compaction indices

Third, current porous concrete preparation methods lack a standardised methodology capable of achieving a constant void content across different mix designs. Without a volumetrically controlled approach, specimens produced from varying mixtures will differ in their final porosity as well as in the specific independent variables under investigation. This co-variation makes it impossible to isolate the individual contributions of the independent variables such as aggregate angularity or paste volume to subsequent mechanical and compaction performance. Porosity therefore acts as an uncontrolled confounding variable rather than a fixed baseline, causing any observed differences in strength or workability between mixtures difficult to be interpreted, as performance changes could only reflect changing void contents rather than true aggregate morphology properties.

However, the SGC allows to evaluate two workability metrics defined by Kevern et al. (2009): the Workability Energy Index (WEI), which quantifies initial flowability, and the Compaction Densification Index (CDI), which quantifies the energy required to reach design density. The b/a ratio governs these indices more strongly than water content adjustments, and aggregate morphology drives paste demand through its influence on specific surface area and inter-particle friction. Despite these individual findings, the combined effect of aggregate angularity and paste volume under 200 kPa compaction has not been investigated in a volumetrically controlled framework.

Previous studies characterising porous concrete workability have relied on low-pressure SGC testing at 60 kPa, which fails to replicate the compaction energy of mechanised slipform placement, and past aggregate morphology studies have frequently introduced mineralogical confounding variables by sourcing rounded and crushed materials from different geological regions. Compounding this, the absence of a volumetrically controlled mix design framework means that specimens across different mixtures have rarely shared a verified, equivalent void content, leaving porosity as an uncontrolled factor in the comparison.

Consequently, the combined effect of aggregate angularity and b/a ratio on fresh-state compaction mechanics and mechanical strength has not been quantified under conditions that simultaneously reflect mechanised placement energy, eliminate mineralogical variability, and enforce a constant void content across the experimental matrix. Without establishing these three controls together, it is not possible to reliably design a porous concrete mixture that self-compacts under heavy mechanised paving operations while guaranteeing target porosity and adequate mechanical strength.

1.3 Objective of the Study

The primary objective of this thesis, executed under the PORO-CITY project framework, is to define a self-compacting porous concrete mixture that balances fresh-state flowability with mechanical strength. By eliminating the need for external mechanical compaction, this research aims to ensure uniform density across permeable pavement sections, addressing the field compaction inconsistencies documented by Kevern et al. (2009).

The study evaluates how coarse aggregate angularity interacts with cementitious paste volume under compaction considering: (i) characterisation of the fresh-state behaviour through WEI and CDI indices under a 200 kPa compaction pressure; (ii) enforcing volumetric equivalence across all specimens using a constant-volume "stop-at-height" methodology during gyratory compaction; and (iii) evaluating properties with 7-day splitting tensile strength.

2. Literature review

2.1 Porous concrete

Porous concrete is a specialised paving material characterised by a high degree of pore connectivity, typically achieving a porosity between 15% and 35% with pore sizes ranging from 2 mm to 8 mm (Adresi et al., 2023). This open-graded structure is achieved by reducing or eliminating the fine aggregate fraction, allowing air and water to pass through interconnected macro-scale voids (Elango and Revathi, 2017). This permeable structure makes porous concrete a viable alternative pavement material, capable of mitigating the environmental consequences of urban stormwater runoff while also addressing vehicle skidding problems (Chockalingam et al., 2023). A visual demonstration of macroscopic interconnectivity and permeability is shown in Figure 2.1.

Figure 2.1: Visual demonstration of porous concrete permeability (Source: Concrete Construction)

Porous concrete initially gained widespread adoption as a building material in Europe following World War II, when raw material scarcity made its lower cement demand attractive (ACI 522 Committee Report, 2006). In the United States, its use expanded significantly in the 1970s in southern states such as Florida, accelerating further after the U.S. Environmental Protection Agency introduced the National Pollutant Discharge Elimination System Phase II requirements (Kevern, 2008).

Today, porous concrete is recognised as an important component of sustainable urban development. It delays the peak of storm events and promotes subgrade infiltration, and during this infiltration process it actively purifies stormwater runoff: primary studies compiled by Adresi et al. (2023) report a significant reduction in dissolved heavy metals, specifically lead, cadmium, zinc, and copper, as water permeates the macro-porous matrix, while petroleum hydrocarbons are metabolised through biological processes within the void network (Kevern, 2008). It also contributes to reducing the Urban Heat Island (UHI) effect through evaporative cooling (Figure 2.2), positioning porous pavement as a key element of the "Sponge City" concept, an urban planning framework aimed at absorbing, filtering, and recycling rainwater (Figure 2.3) (Adresi et al., 2023). Finally, its open surface texture diffuses tire-pavement interaction noise, making it one of the quietest available paving options (Kevern, 2008).

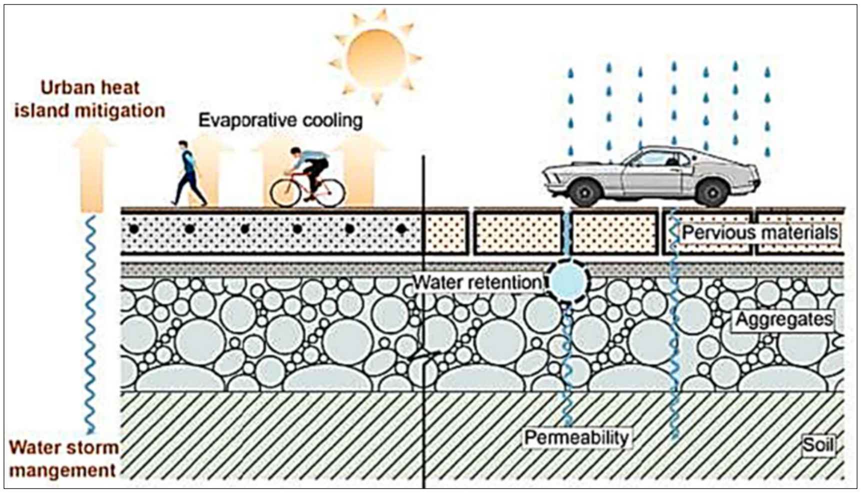

Figure 2.2: effects of pervious pavements on urban heat island (UHI) mitigation and water storm runoff control (adapted from J. Wang et al. 2022, as compiled by Adresi et al. 2023)

Figure 2.3: Comprehensive operational framework and blue-green infrastructure components defining the "Sponge City" concept (adapted from Xu et al. 2018, as compiled by Adresi et al. 2023).

2.2 Mechanical and physical properties

The physical and mechanical behaviour of porous concrete is fundamentally different from that of conventional concrete, governed by a direct inverse relationship between porosity and mechanical strength (Adresi et al., 2023). As void content decreases, the interparticle contact area between paste-coated aggregates increases, resulting in higher load-carrying capacity (Schaefer et al., 2006); because high porosity must nonetheless be maintained for adequate permeability, compressive strength is generally restricted to a range of 2.8 MPa to 28 MPa (Adresi et al., 2023).

Tensile and flexural performance follow a similar dependence on the paste-aggregate bond. Splitting tensile strength is generally between 12% and 15% of compressive strength (Schaefer et al., 2006), though measured values vary: Chockalingam et al. (2023) report average splitting tensile and flexural strengths of 17% and 32% of cube compressive strength respectively (or 15% and 34% of cylinder compressive strength), while Chen et al. (2013) place flexural strength between 1.5 MPa and 3.2 MPa, heavily dependent on paste thickness and the quality of the aggregate-to-paste bond. An empirical correlation between compressive and splitting tensile strength, established by Ibrahim et al. (2014), is shown in Figure 2.4.

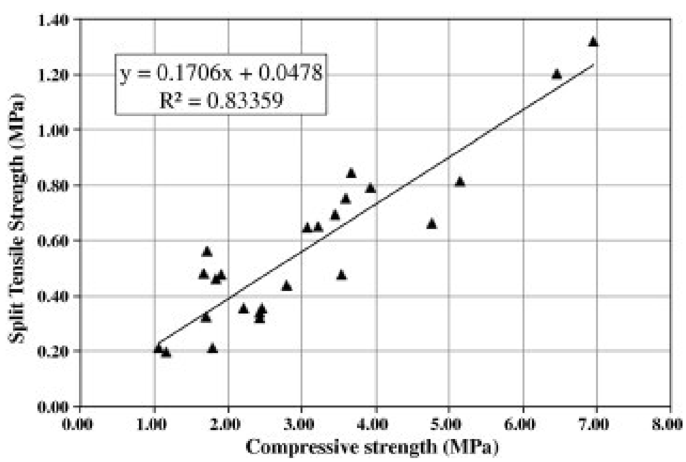

Figure 2.4: Empirical correlation between compressive strength and splitting tensile strength of Portland cement porous concrete mixtures (adapted from Ibrahim et al. 2014).

The mechanism behind this bond dependence has been examined directly at the failure surface. Using 2D and 3D CT imaging of specimens under compressive loading, Yu et al. (2019) found that cracks predominantly initiate at the interfacial transition zone (ITZ) between the cement slurry and the aggregate, confirming that bond strength at this interface is a critical factor governing compressive performance; compressive strength proved highly sensitive to the content of small pores in the 0–1.5 mm² range, with an increase in these pores substantially reducing matrix strength.

Specimen and aggregate size introduce a further, related effect. Chockalingam et al. (2023) show that increasing both specimen size and aggregate size reduces compressive, splitting tensile, and flexural strength, since smaller aggregates reduce the distance between particle contact points, forcing cracks to deflect around aggregates and thereby requiring more energy to propagate failure than in mixtures with larger aggregates. This relationship between aggregate size, specimen height, and ultimate tensile strength is shown in Figure 2.5.

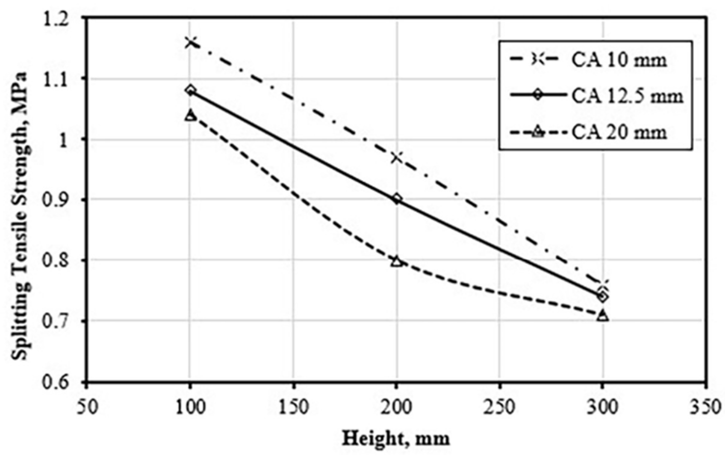

(a) Splitting Tensile Strength vs. Height

Figure 2.5: Influence of aggregate size and specimen height on the splitting tensile strength of porous concrete (adapted from Chockalingam et al. 2023).

2.3 Porous concrete mix design approaches

Unlike conventional concrete, porous concrete lacks a singular, universally accepted mix design standard. Adresi et al. (2023) observe that researchers and engineers frequently rely on trial-and-error methodologies to balance mechanical resistance against hydraulic permeability, drawing on foundational guidelines such as those of the ACI 522 committee. A persistent limitation of these early guidelines, including those of the PCA and NRMCA (Tennis et al., 2004), is that they do not adequately account for the role of compaction energy on the final void content, nor do they provide clear guidance on determining an optimal water-to-cement (w/c) ratio for a given aggregate and binder combination, a gap explicitly noted by Nguyen et al. (2014).

A further challenge in mix design evaluation is measuring fresh-state consistency. Kevern et al. (2009) point out that the traditional slump test used for conventional concrete is entirely ineffective for the porous mixtures. Mrakovčić et al. (2014) confirmed this limitation, observing that standard compaction by vibration causes immediate paste segregation to the bottom of the mould; instead, they validated a manual clump shaping method to assess fresh consistency. However, Kevern et al. (2009) argue that visual and manual assessments lack the quantifiable data needed for reliable quality control in large-scale applications, and that a more scientific, performance-based approach is urgently required.

To address this gap, Kevern et al. (2009) introduced the SGC as a workability characterisation tool for porous concrete. The methodology extracts two performance indices from the compaction curve which define the fresh-state placement of a mixture. The theoretical foundations, operational parameters, and classification thresholds of this methodology are discussed in detail in Section 2.5.

When optimizing mix proportions, the volume and viscosity of the cementitious paste serve as the dominant variables. Kevern et al. (2009), as shown in Figure 2.6, demonstrated that increasing the binder-to-aggregate (b/a) ratio improves initial workability (WEI) and triggers a sharp reduction in required compaction energy (CDI) far more effectively than merely adjusting the water content. When sufficient binder is present, the paste acts as a lubricant between aggregate particles, separating them and reducing inter-particle friction. By fixing a stable w/c ratio, for example 0.29 in mixes, and then adjusting the b/a ratio, a consistent paste coating thickness can be maintained across the aggregate skeleton without inducing paste drainage or clogging the functional macro-pores (Figure 2.7).

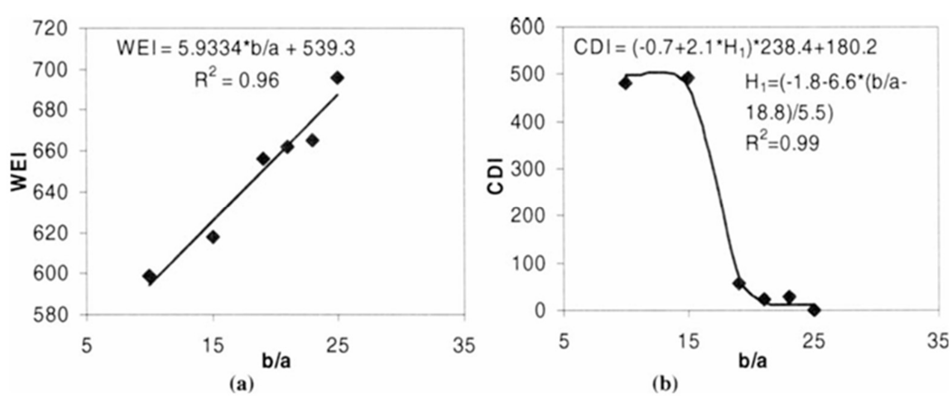

Figure 2.6: Effect of binder-to-aggregate (b/a) mass ratio on the workability and compactibility indices of porous concrete mixtures (adapted from Kevern et al. 2009).

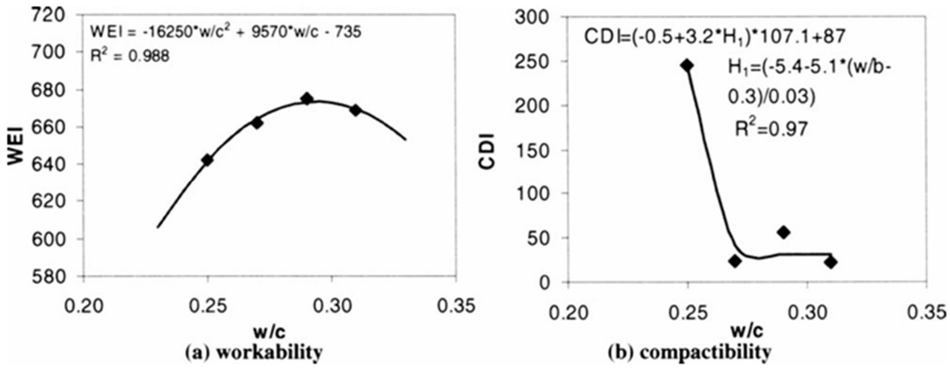

Figure 2.7: Effects of water-to-cement (w/c ratio on the workability and compactibility indices of porous concrete mixtures (adapted from Kevern et al. 2009).

2.4 The role of aggregate characteristics

Because the aggregate matrix forms the primary load-bearing skeleton of porous concrete, the physical dimensions and the morphology of the particles directly govern the final performance of the pavement. Coarse aggregate is the largest single constituent by volume in a pervious concrete mixture.

Elango and Revathi (2017) found that increasing coarse aggregate size systematically increases porosity and permeability while reducing density and compressive strength. Yu et al. (2019) provide a more precise threshold through CT scanning: as plotted in Figure 2.8, compressive strength increases rapidly as aggregate size increases up to approximately 7 mm, beyond which further size increases produce no significant strength gain. They also established that cementitious paste thickness increases with aggregate size, stabilizing once the paste layer reaches approximately 1.15 mm. These findings provide direct support for adopting a narrow 4–8 mm aggregate grading, which simultaneously optimises paste coating thickness and compressive strength.

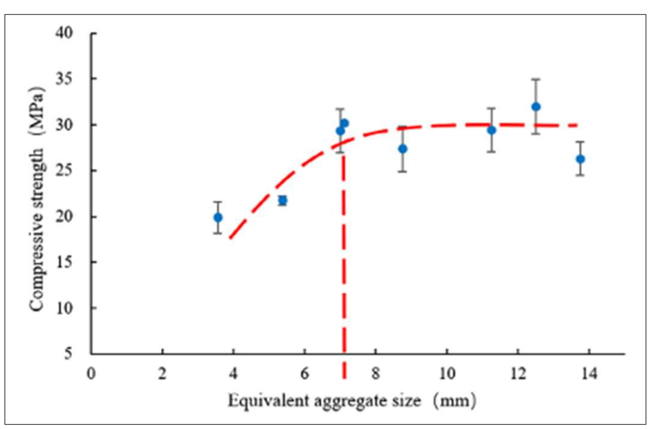

Figure 2.8: Effect of aggregate size on compressive strength of porous concrete (adapted from Yu et al. 2019).

In terms of particle shape, Chinchillas-Chinchillas et al. (2014) report that mixtures containing irregular, angular aggregates exhibit higher physical strength due to the increased adhesion between the cement paste and the rough aggregate surfaces. On the other hand, Kevern (2008) cautions that angular aggregates have a larger specific surface area and higher inter-particle friction than rounded river gravel, both of which resist compaction and demand more cementitious paste to achieve adequate lubrication during placement.

To manage the frictional resistance of angular aggregates without affecting the void content, researchers have investigated the selective reintroduction of fine aggregates. Kevern (2008) established a combined gradation framework defining the upper and lower boundaries for single-sized coarse aggregates alongside a designated envelope for fine aggregate additions (Figure 2.9). Within this distribution scheme, Kevern (2008) found that adding a small percentage of sand, approximately 5% to 7% by weight of the coarse aggregate, increases the volume and viscosity of the cement mortar, allowing coarse particles to support a thicker paste layer.

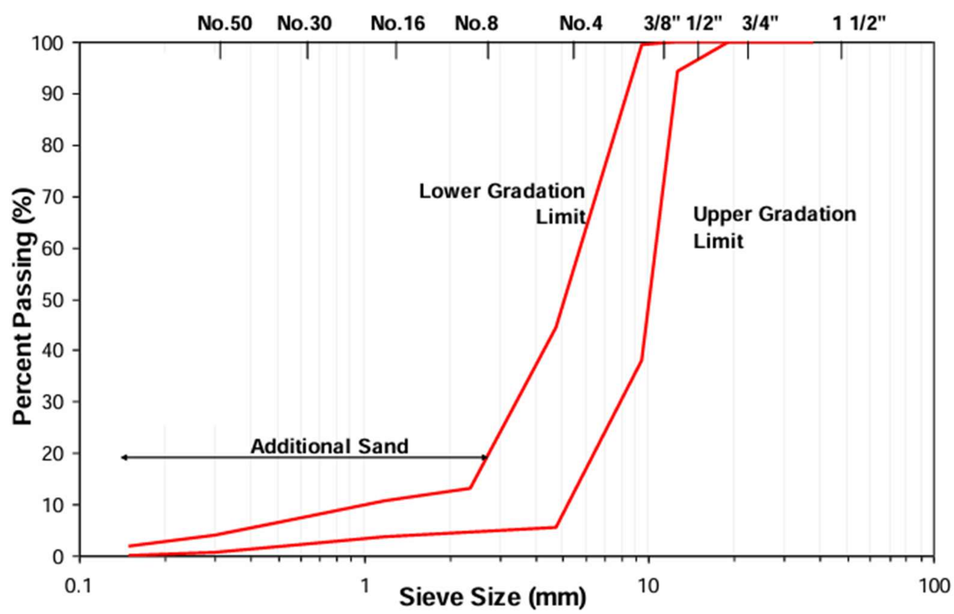

Figure 2.9: Combined coarse aggregate gradation limits and fine aggregate (sand) addition envelope for pervious concrete mixtures (adapted from Kevern 2008).

Moreover, Adresi et al. (2023) confirm that fine aggregates in the range of 5% to 10% of total volume can boost concrete strength without critically closing the drainage pores. Mrakovčić et al. (2014) further demonstrated experimentally that while eliminating fine aggregates entirely maximises permeability, additions of up to 15% fine sand (0–2 mm fraction) significantly enhance compressive strength while keeping hydraulic properties within acceptable limits.

This consensus supports the use of a constant 5% sand-to-aggregate mass ratio to stabilise the matrix and enhance structural capacity.

In the context of pervious concrete pavement, aggregate angularity refers to the shape and surface texture of mechanically fractured stones, distinguishing them from naturally water-worn, near-spherical river gravels (Figure 2.10, Kevern, 2008). This property is treated in this thesis as a primary independent variable, since it affects both the fresh-state rheology and the mechanical performance of open-graded cementitious matrices (Kevern et al., 2009; Adresi et al., 2023).

Figure 2.10: Qualitative classification of coarse aggregate morphological profiles showing rounded (left), semi-angular (centre), and angular (right) aggregate angularity (adapted from Kevern, 2008).

Aggregate angularity affects the porous concrete in two main ways:

- **Fresh-state rheology and paste demand:** for particles of the same nominal size, a crushed aggregate has more surface area than a rounded one, and workability in porous concrete depends on mortar lubrication between particles. A mixture with higher aggregate angularity therefore requires more paste to reach the same workability as a smoother aggregate mixture (Kevern, 2008).

- **Interfacial bond and failure mode:** angular aggregate with a rough texture has better bond characteristics than smooth aggregate (Kevern, 2008), and mixtures with irregular, angular aggregates have been shown to reach higher strength because of increased adhesion between the cement paste and the aggregate surface (Chinchillas-Chinchillas et al., 2014). This trend is not universal, however: Jain and Chouhan (2011) found the opposite relationship for compressive strength, it decreased as their measured angularity number increased, while permeability increased. The relationship between angularity and bond strength is therefore not fully settled in the literature, which is part of the gap this thesis addresses.

2.5 Workability and compaction

As introduced in Section 2.3, Kevern et al. (2009) pioneered the use of the SGC for workability characterisation of porous concrete specimens. The compaction curve produced by the SGC has two distinct portions. The first, characterised by a steep slope, captures the rapid removal of excess air voids under initial compaction and reflects the intrinsic self-compacting ability of the mixture. The second portion, characterised by a shallower slope, captures the resistance of the aggregate skeleton to further densification as particles rearrange.

These two regions form the basis for the two workability indices defined by Kevern et al. (2009): the Workability Energy Index (WEI), calculated as the area under the compaction curve from one to eight gyrations, and the Compaction Densification Index (CDI), calculated as the area under the curve from eight gyrations to the Design Void Content (DVC) or 100 gyrations, whichever occurs first. Together, WEI and CDI constitute what Kevern et al. (2009) term the placement of a porous concrete mixture, as illustrated in Figure 2.11.

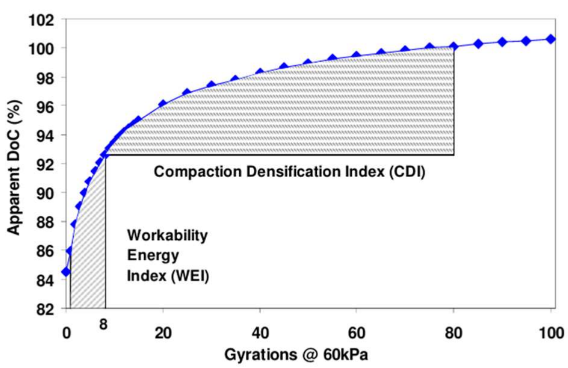

Workability (WEI) Explanation	Range
Self-Consolidating	> 640
Acceptable Workability	640>WEI>600
Poor Workability	WEI<600

Compactibility (CDI) Explanation	Range
No Additional Compaction Required	CDI<50
Normal Compaction Effort Required	50<CDI<450
Considerable Additional Compaction Effort Required	CDI>450

Figure 2.11: Definition of gyratory workability indices and reference performance ranges for fresh pervious concrete mixtures (adapted from Kevern et al. 2009).

In establishing this methodology, Kevern et al. (2009) modified a standard asphalt SGC unit by removing its high-pressure hydraulic orifice, reducing the vertical compaction pressure from the standard asphalt industry value of 600 kPa to 60 kPa. This lower pressure was selected to replicate the minimal energy imparted by manual hand rollers and lightweight screeds — the placement methods dominant at the time. Based on the classification thresholds developed from this 60 kPa testing program, Kevern et al. (2009) established that a WEI above 640 indicates a highly workable, self-compacting mixture, while a CDI below 50 indicates that the mixture requires no additional compaction energy to reach the DVC.

However, porous concrete for pervious road pavements is increasingly placed using slipform pavers, which impose higher compaction energy than hand rollers or roller-screeds. Operating the SGC at the unmodified laboratory pressure of 200 kPa therefore serves as a more representative proxy for these mechanised conditions.

A further limitation of traditional SGC approaches is their reliance on a fixed number of gyrations, which allows final specimen porosity to fluctuate with mix stiffness. Since mechanical strength in porous concrete is inversely proportional to void content, this density variation acts as a confounding variable that makes direct comparison between mixes unreliable. A constant-volume "stop-at-height" methodology overcomes this by calculating the exact constituent masses required for a target design void content (DVC) and commanding the SGC to halt compaction the moment the specimen reaches a predetermined height. This ensures that all specimens across the experimental matrix share identical void contents, fully isolating the effects of the variables under investigation.

Following compaction and a standard 7-day moisture curing period, the porosity of each specimen must be verified independently. For this purpose, Montes et al. (2005) developed a standardised water-displacement procedure based on Archimedes' principle, calculating total porosity from the difference in weight between oven-dried and submerged specimens. Kevern et al. (2009) adopted this procedure as the standard porosity verification method in their gyratory compaction framework. Once the void content is confirmed, the structural integrity of the cylinder can be evaluated through indirect tensile testing, providing a direct measure of the hardened mechanical performance of each mix design.

2.6 Research gap

A review of the literature reveals that the individual parameters governing porous concrete performance have been extensively documented, yet their combined interaction under mechanised placement conditions remains unexplored.

Despite these individual findings, a critical gap remains in the literature regarding the interacting mechanics of aggregate angularity and paste volume under high-energy mechanised compaction. Kevern et al. (2009) identified the effect of aggregate angularity on porous concrete workability as a key direction for future research. Previous studies relying on 60 kPa compaction do not capture the true locking point of angular aggregates under slipform paving forces. Furthermore, studies comparing aggregate morphologies have often sourced rounded and crushed materials from different geological regions, introducing mineralogical confounding variables that make direct comparison unreliable.

To fill this gap, this research proposes a comprehensive experimental investigation evaluating three b/a ratios (18%, 21%, and 24%) against three aggregate angularity profiles (100% rounded, 100% crushed, and a 50/50 blend). To eliminate mineralogical variability, all coarse aggregates (4–8 mm) and fine sand (0–2 mm) are sourced from the same geological quarry and subjected to a full suite of characterisation tests, including apparent particle density, oven-dried and saturated surface-dried particle density, water absorption, dry rodded bulk density, compacted and uncompacted voids, flakiness index, and shape index.

By standardising cement type (Type II 42.5R), w/c ratio (0.29), superplasticizer dosage (1%), and DVC (20%), the precise thresholds at which different aggregate morphologies reach a self-compacting state under 200 kPa of compaction pressure can be isolated. Validating the porosity via the Montes et al. (2005) water-displacement procedure and assessing the ultimate tensile strength will allow engineers to optimally balance aggregate angularity and paste volume, yielding a porous concrete mixture that self-compacts for slipform paving and yields an acceptable mechanical strength.

3. Materials and methods

3.1 Objectives and experimental program

The primary objective of this experimental program is to define a porous concrete mixture that self-compacts under mechanised placement, specifically slipform paving, while simultaneously maintaining adequate mechanical strength. To identify the physical thresholds at which this balance is achieved, the study investigates the combined effect of coarse aggregate angularity and cementitious paste volume under gyratory compaction.

A 3×3 experimental matrix was designed, producing nine distinct mix configurations. Two independent variables were evaluated:

- Coarse Aggregate Angularity: Three morphological profiles were tested — 100% rounded river gravel, 100% crushed aggregate, and a 50/50 blend by mass — to assess the influence of internal friction and particle interlock on compaction behaviour.
- Binder-to-Aggregate (b/a) Mass Ratio: Each aggregate profile was tested at three b/a ratios — 18%, 21%, and 24% — to determine the paste volume required to adequately lubricate each aggregate skeleton and bridge the intraparticle voids.

All other mixture parameters were held constant throughout the experimental campaign to ensure that observed variations in workability and mechanical performance are attributable solely to these two variables. The fixed parameters are as follows:

- Design Void Content (DVC): Fixed at 20% across all mixtures using the absolute volume mix design method.
- Aggregate Grading: A narrow coarse aggregate grading of 4–8 mm was used to optimise paste coating thickness and minimise the aggregate size effect on mechanical performance.
- Fine Aggregate: A fine sand (0–2 mm) was incorporated at a constant mass ratio of 5% of the coarse aggregate to stabilise the matrix without clogging the macro-pores.
- Binder: Portland Cement Type II 42.5R (EN 197-1) was used for all mixes.
- Water-to-Cement (w/c) Ratio: Fixed at 0.29 to produce a stable, viscous paste resistant to vertical drainage during compaction.

- Superplasticizer: A high-range water reducer was maintained at 1% by mass of the cementitious binder.

- Compaction Energy: All specimens were compacted using a SGC at a vertical pressure of 200 kPa, to simulate mechanised slipform placement and engage the aggregate locking point.

For each of the nine mix designs, three replicate cylindrical specimens were produced. The experimental program is divided into two phases. In the first, fresh-state workability is characterised dynamically during SGC compaction through the WEI and the CDI. In the second, following a 7-day moisture curing period, the hardened state is evaluated by verifying the true porosity via a water-displacement procedure and by measuring the ultimate splitting tensile strength.

3.2 Materials

3.2.1 Cement

A commercially available Portland-composite cement conforming to the European Standard EN 197-1 classification Type II 42.5R was used for all mixtures. The “Type II” designation indicates a Portland-composite cement containing a controlled proportion of secondary constituents alongside Portland clinker, which moderately reduces the heat of hydration relative to pure Type I cement. The “42.5” designation specifies a minimum characteristic compressive strength of 42.5 MPa at 28 days, ensuring the paste has the mechanical capacity required for structural applications. The “R” designation indicates rapid early strength development, which stabilises the aggregate-paste bonds in the first hours of hydration, limiting the risk of paste drain-down before initial set, and is consistent with the 7-day testing cycle used in this program.

3.2.2 Aggregates

A narrow, single-sized coarse aggregate grading of 4–8 mm was used across all mix designs. This selection is supported directly by the literature (Yu et al., 2019; Chockalingam et al., 2023).

To eliminate mineralogical variability as a confounding factor, all mineral aggregates — fine sand, rounded coarse aggregate, and crushed coarse aggregate — were sourced from the same supplier and location: Cave Germaire S.p.A., Carignano, Turin, Italy. According to the manufacturer’s Declarations of Performance (DoP 001, DoP 006, and DoP 020), the entire aggregate supply shares a uniform petrographic composition, comprising principal metamorphic lithotypes including mica schist, gneiss, quartzite, calc-silicates (calcefiri), and lithic fragments attributable to granites and granodiorites. All aggregates are also certified under UNI 8520-22:2020 as non-reactive to the alkali-silica reaction (RA2 — Aggregato Non Reattivo), ensuring the long-term chemical stability of the matrix. Before using the aggregates in the mixtures, all coarse aggregates were washed to eliminate contaminants and fine particles. The morphological profiles of both the *Risino* and *Graniglia* are displayed in Figure 3.1.

Figure 3.1: Morphological profiles of (a) *Risino* (100% rounded aggregate) exhibiting smooth geometry coarse aggregate fractions, and (b) *Graniglia* (100% crushed aggregate) displaying high angularity and surface roughness (adapted from Cave Germaire).

Fine aggregate (0–2 mm Sand)

The fine aggregate fraction used to stabilise the paste without compromising hydraulic permeability is commercially designated by Cave Germaire as "*Sabbia Fine*" (Fine Sand). It conforms to EN 12620 and EN 13139, with a continuous particle size distribution from 0 to 2 mm.

Rounded coarse aggregate (2–8 mm "Risino")

The rounded aggregate variable was fulfilled using naturally shaped river gravel, commercially designated as "*Risino* 2/8". Prior to batching, the material was sieved in the laboratory to strict 4–8 mm boundaries, discarding particles outside this range.

Crushed coarse aggregate (3–8 mm "Graniglia")

The crushed aggregate variable was fulfilled using mechanically fractured stone, commercially designated as "*Graniglia* 3/8". This material was likewise sieved in the laboratory to isolate the 4–8 mm fraction.

3.2.3 Chemical admixtures

To maintain the w/c ratio at 0.29 while retaining adequate fresh-state flowability under compaction, a high-range water-reducing (HRWR) admixture was employed. As Kevern et al.

(2009) observed, porous concrete is usually produced within a narrow w/c window of 0.27 to 0.33. Below this range the paste lacks the cohesion to coat the aggregates, while above it the paste drains away from the aggregate surfaces and permanently clogs the load-carrying macro-pores. A superplasticizer allows the required paste viscosity to be maintained at the low w/c of 0.29 without resorting to additional water. The dosage was held constant at 1.0% by mass of the cementitious binder across all nine mixtures (Bassani et al., 2022).

3.3 Aggregate characterisation

To ensure absolute volumetric precision in the mix design calculations, a comprehensive laboratory characterisation program was conducted on the specific aggregate batches supplied for this study. Given that the w/c ratio of 0.29 operates within a narrow functional window of 0.27 to 0.33 (Kevern et al., 2009), obtaining precise particle density and water absorption values is therefore critical.

The program evaluated particle density and water absorption, geometric shape parameters, and aggregate void content. Furthermore, since the entire experimental program rests on the premise that the *Risino* and *Graniglia* aggregates differ meaningfully in angularity while sharing the same mineralogy, the shape characterisation tests provide the quantitative morphological evidence that justifies treating the two materials as genuinely distinct independent variable levels.

3.3.1 Particle density and water absorption (pycnometer test)

The apparent particle density (ρa), oven-dry particle density (ρrd), saturated surface-dry particle density (ρssd), and 24-hour water absorption (WA_{24}) of all three aggregate fractions were determined by the pycnometer method in accordance with EN 1097-6. All three are required inputs for the absolute volume mix design equations in Section 3.4.1. The execution of this testing, involving vacuum de-airing flasks and final saturated surface-dry conditioning, is shown in Figure 3.2. The resulting parameters are reported and verified within Section 4.1.

Figure 3.2: Laboratory procedure for determining the particle density and water absorption of aggregates in accordance with EN 1097-6: (a) vacuum de-airing of submerged samples within pycnometer flasks, and (b) conditioning of coarse aggregate particles to a Saturated Surface Dry (SSD) state

3.3.2 Particle shape characterisation

Two complementary shape indices were determined to quantify the morphological difference between the *Risino* and *Graniglia* aggregates. The Flakiness Index (FI) was determined in accordance with EN 933-3. The FI quantifies the proportion by mass of particles whose minimum dimension is less than 0.6 times the mean sieve size of the fraction; a lower value indicates more equidimensional particles. For the 4–8 mm fraction, as displayed in Figure 3.3, the test was applied across three sub-fractions (6.3/8 mm, 5/6.3 mm, and 4/5 mm) using square-aperture sieves and corresponding bar sieves with slot widths of 4 mm, 3.15 mm, and 2.5 mm, respectively. Sample reduction to the required minimum test portion of 0.6 kg was performed by quartering in accordance with EN 932-2.

Figure 3.3: Laboratory procedure for determining the Flakiness Index (FI) of coarse aggregate fractions in accordance with EN 933-3: (a) mechanical separation into size sub-fractions, and (b) thickness gauging using parallel bar sieves.

The Shape Index (SI) was determined in accordance with EN 933-4. The SI quantifies the proportion by mass of particles whose length-to-thickness ratio exceeds 3; a higher value indicates a greater proportion of elongated particles that reduce packing efficiency and increase inter-particle friction. Together, FI and SI provide complementary characterisation: FI detects thinness in the narrowest dimension, SI detects elongation in the longest. The assessment of particle elongation via calliper testing is pictured in Figure 3.4, and the results are compiled in Section 4.1.

Figure 3.4: Evaluation of coarse aggregate particle elongation using a specialised calliper in accordance with EN 933-4.

3.3.3 Aggregate void content

The compacted (rodded) and uncompacted void contents of both coarse aggregate fractions were determined in accordance with ASTM C29/C29M and EN 1097-3 respectively. The compacted void content was obtained by filling a standardised cylindrical container in three equal layers, each subjected to 25 rodding strikes, before measuring the bulk density; the uncompacted void content was obtained by filling the same container without any external compaction, as illustrated in Figure 3.5. Both void parameters were derived from the measured bulk densities and the oven-dry particle densities determined in Section 3.3.1, with results compiled in Section 4.1.

Figure 3.5: Laboratory test configuration for determining the uncompacted (loose) bulk density and void content of coarse aggregate fractions in accordance with EN 1097-3.

3.4 Laboratory mix design procedure

3.4.1 The absolute volume method

Porous concrete must be proportioned to guarantee a specific target porosity rather than to maximise density. The mix designs in this research were therefore developed using the absolute volume method, which enforces the Design Void Content (DVC) by requiring that the sum of the absolute volumes of all solid constituents — coarse aggregate, fine aggregate, cement, and water — plus the targeted void space equals exactly one unit volume (1.0 m^3). The fundamental volumetric balance equation is:

$$V_{agg} + V_{binder} + V_{water} + V_{void} = 1.0 \qquad (3.1)$$

By fixing V_{void} at 0.20 to enforce the 20% DVC and substituting the specific gravities of each constituent as determined through the pycnometer tests in Section 3.3.1, the exact required constituent masses are derived. This volumetric equilibrium can also be expressed to isolate the total solid fraction:

$$V_{agg} + V_{binder} + V_{water} = (1 - DVC) \times V_{total} \quad (3.2)$$

This approach eliminates the variability inherent in mass-based empirical guidelines, which do not account for the specific gravities of the raw materials and therefore produce unpredictable final void contents.

3.4.2 Mixture Proportions

Nine distinct mixture proportions were calculated considering the three b/a ratios (18%, 21%, and 24%) across three aggregate angularity profiles (100% rounded *Risino*, 100% crushed *Graniglia*, and a 50/50 blend). The following parameters were held constant across all nine designs: w/c ratio fixed at 0.29; fine sand content fixed at 5% of the total coarse aggregate mass; superplasticizer fixed at 1.0% of cement mass; and target porosity of 20%.

The total required batch mass for each mix was governed by the internal dimensions of the SGC cylindrical moulds combined with the stop-at-height compaction methodology. With a fixed mould diameter of 100 mm and a target compaction height of 100 mm, the final specimen volume is exactly 785.4 cm³. The target batch mass for each design was calculated from this volume by isolating the aggregate mass in the volumetric balance of Equation 3.2 and substituting the fixed mixture ratios together with the laboratory-measured particle densities from Section 4.1:

$$M_{agg} \times \left(\frac{1}{\rho_{agg}} + \frac{s/a}{\rho_{sand}} + \frac{b/a}{\rho_c} + \frac{(b/a) \times (w/c)}{\rho_w} \right) = (1 - DVC) \times V_{total} \quad (3.3)$$

where M_{agg} is the total coarse aggregate mass per specimen; s/a and b/a are the fixed sand-aggregate and binder-aggregate mass ratios; w/c is the water-cement ratio (0.29); ρ_{agg}, ρ_{sand}, ρ_c, and ρ_w are the particle densities of the coarse aggregate, fine sand, cement, and water, respectively (Section 4.1); DVC is the Design Void Content (20%); and V_{total} is the target specimen volume (785.4 cm³). Equation 3.3 was solved for M_{agg} for each of the nine mix combinations, after which the corresponding sand, binder, and water masses were derived directly from the fixed ratios. These values are summarised in Table 3.1.

The two independent variables—coarse aggregate morphology (rounded river gravel R, crushed aggregate C, and blended M) and binder-to-aggregate mass ratio (18%, 21%, and

24%)—were combined to construct the nine design mixtures (R18, R21, R24, M18, M21, M24, C18, C21, and C24).

Table 3.1: mix design proportions and unit weights per 100 × 100 mm cylindrical specimen to achieve a 20% Design Void Content.

Mixture Group	b/a (%)	M agg (g)	M sand (g)	M cement (g)	M water (g)	Unit Weight of the Fresh Concrete (kg/m3)
R18 / M18 / C18	18	1195	60	226	66	1997.1
R21 / M21 / C21	21	1153	58	254	74	1987.0
R24 / M24 / C24	24	1114	56	281	81	1977.6

3.5 Specimen preparation and compaction

3.5.1 Mixing protocol

Prior to mixing, all mineral aggregates were conditioned to the Saturated Surface Dry (SSD) state to prevent the dry pores from absorbing mixing water, which would otherwise reduce the effective w/c ratio below the target of 0.29 (Kevern et al., 2009). The SSD pre-wetting quantities were calculated using the WA24 values presented in Section 4.1: 1.2% for both coarse aggregate fractions and 1.4% for the fine sand. Figure 3.6 shows the conditioned aggregate batch in the SSD state, ready for the mixing phase.

The mixing sequence followed the standard practice for making and curing concrete test specimens (ASTM C192):

1. The SSD coarse aggregate, fine sand, cement, and approximately two-thirds of the design water were introduced into the mechanical mixer and blended for 30 seconds.

2. The remaining one-third of the water, pre-mixed with the superplasticizer (1% by mass of binder), was gradually added. The mixture was then agitated for 3 minutes.

3. The mixer was stopped and the concrete rested for 3 minutes to allow initial activation of the superplasticizer.

4. The mixer was restarted for an additional 2 minutes of continuous mixing to complete paste homogenization and finalise coating of the aggregate skeleton (Figure 3.7).

Figure 3.6: Coarse and fine aggregate batch prepared in the Saturated Surface Dry (SSD) state prior to the mixing phase.

Figure 3.7: Freshly mixed porous concrete displaying uniform paste coating prior to transfer into the SGC mould.

3.5.2 Compaction with Superpave Gyratory Compactor

Immediately after mixing, the fresh mixture was transferred to the Superpave Gyratory Compactor (SGC) using cylindrical steel moulds. The constant-volume stop-at-height approach was applied to enforce the 20% DVC, targeting the baseline specimen volume ($V_{\text{total}} = 785.4 \text{ cm}^3$) derived in Section 3.4.2.

Once the calculated mass was loaded into the mould, the SGC was initialised at a constant vertical pressure of 200 kPa. As discussed in Section 1.2, this pressure is used to simulate the energy of mechanised slipform placement and to fully engage the aggregate skeleton, allowing the mechanical locking point to be identified. The machine recorded the specimen height throughout the gyration process and was programmed to stop the moment the height reached 100 mm. The WEI was extracted from the energy consumed during the initial gyration phase, and the CDI was calculated as the total energy required to reach the 100 mm target height. An image of the freshly compacted cylinder immediately upon extrusion from the SGC machine is shown in Figure 3.8.

Figure 3.8: Freshly extruded porous concrete specimen following gyratory compaction, prepared for transfer to the moisture-controlled curing chamber.

3.5.3 Analysis of compaction curves

To establish a performance-based workability framework that replaces subjective field assessments, this study processes the continuous raw data generated during gyratory compaction. For each prepared specimen, the SGC records the specimen height, denoted as h(N), at every gyration N. Because the internal diameter of the steel mould is fixed at 100 mm, this continuous height recording provides the specimen's densification path from its initial loose state to its final state at the target void content.

From the height recording, a dimensionless metric termed the Degree of Compaction, C(N), is derived for each gyration:

$$C(N) = \frac{h_{target}}{h_N} \times 100 \qquad (3.4)$$

where C(N) is the Degree of Compaction at gyration N, expressed as a percentage. When the specimen height equals h_{target}, C(N) reaches 100%, indicating that the specimen has been compacted to its DVC of 20%. Plotting C(N) against the gyration number N yields the compaction curve, an example of which for specimen C21 is shown in Figure 3.9. The curve begins steeply during the initial gyrations, then flattens progressively as the aggregate skeleton resists further compaction.

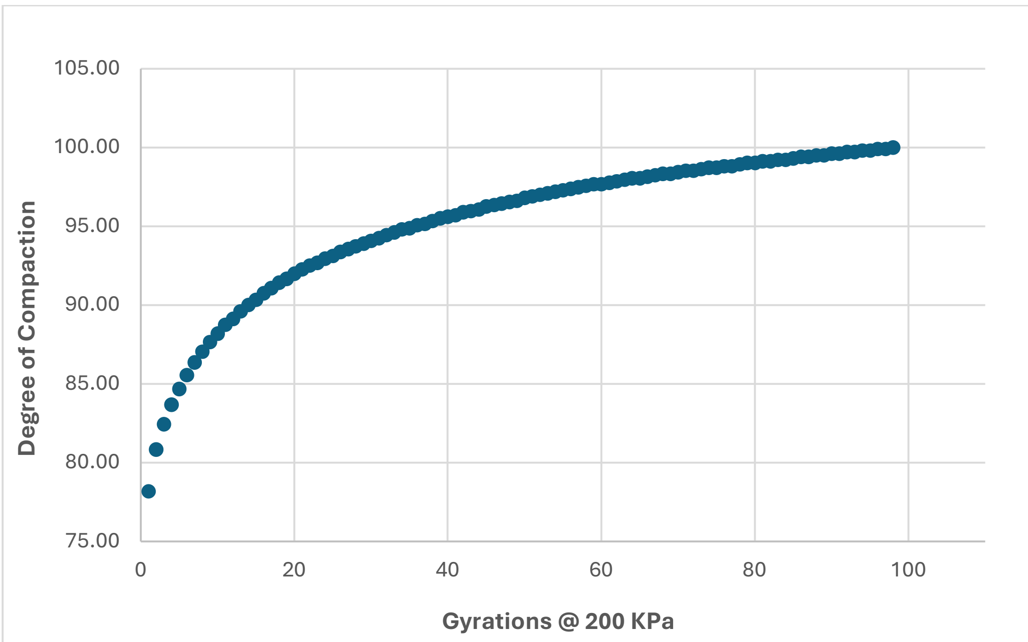

Figure 3.9: Gyratory compaction curve for the 100% crushed aggregate mixture at a 21% binder-to-aggregate ratio (Specimen C21) under the pressure of 200 kPa.

The Workability Energy Index (WEI) and the Compaction Densification Index (CDI) are both computed as areas under this compaction curve, following the framework introduced by Kevern et al. (2009). The WEI captures the initial self-compacting feature of the fresh mixture and is defined as the area under the C(N) curve from gyration 1 to gyration 8:

$$WEI = \int_1^8 C\,(N)\,dN \qquad (3.5)$$

A higher WEI reflects a steeper compaction curve in this initial zone, indicating a mixture with high inherent flowability that densifies rapidly under minimal compaction effort. The CDI quantifies the sustained compaction energy required after this initial phase, from gyration 8 to the point at which the specimen reaches the target height (i.e., C(N) = 100%), or up to a maximum of 200 gyrations if the target is not reached within that limit:

$$CDI = \int_{8}^{N_{final}} [100 - C(N)]\ dN \qquad (3.6)$$

where N_{final} is the gyration at which C(N) first reaches 100%, or 200 if the target height is never reached. A lower CDI is operationally desirable, indicating that the mixture reaches its design void content with lower sustained compaction effort which is a requirement for self-compacting behavior under slipform paving. A mixture classified as compaction refusal never reaches C(N) = 100%, and its CDI is therefore computed over the full 200-gyration run without a natural terminal point.

Because the laboratory SGC captures data at discrete gyration increments ($\Delta N = 1$) rather than a continuous function, the definitive integrals must be resolved numerically. In this research, the Trapezoidal method has been used to approximate the area under the curves.

$$WEI \approx \sum_{N=1}^{7} \left[\frac{C(N)+C(N+1)}{2}\right] \qquad (3.7)$$

$$CDI \approx \sum_{N=8}^{N_{final}-1} \left[\frac{(100-C(N))+(100-C(N+1))}{2}\right] \qquad (3.8)$$

Two aspects of this implementation deviate deliberately from the original Kevern et al. (2009) framework and must be noted explicitly. First, Kevern et al. (2009) defined the Degree of Compaction using a density-based ratio: the unit weight at gyration N divided by the unit weight at the Design Void Content. In the present study, because all specimens are compacted in a fixed-diameter mould under a stop-at-height constraint, the unit weight is uniquely determined by specimen height at every gyration.

$$C(N) = \frac{\rho(N)}{\rho_{target}} \times 100 = \frac{\frac{M}{V(N)}}{\frac{M}{V_{target}}} \times 100 = \frac{V_{target}}{V(N)} \times 100 = \frac{A \cdot h_{target}}{A \cdot h(N)} \times 100 = \frac{h_{target}}{h(N)} \times 100$$

The height-ratio formulation in Equation 3.4 is therefore mathematically equivalent to the density-based formulation but is derived directly from the raw SGC output without requiring any density calculations. Second, Kevern et al. (2009) set a terminal gyration limit of 100; this study extends that limit to 200 gyrations to accommodate the higher compaction resistance of angular aggregate skeletons under 200 kPa pressure and to allow a full characterisation of refusal-class mixes such as C18.

Because both deviations, the higher operating pressure and the extended gyration limit, alter the numerical scale of the resulting indices, the WEI and CDI threshold values established by Kevern et al. (2009) at 60 kPa and 100 gyrations are not directly transferable to this study (Figure 2.11). The indices are therefore interpreted comparatively across the nine mix designs and in terms of the physical mechanisms they reflect, rather than against Kevern's absolute classification thresholds. A detailed comparative analysis and the placeability classification framework developed from this dataset are presented in Section 4.2 and Section 5.4. Additionally, the complete set of gyratory compaction curves for all tested specimens is reported in Appendix A.

3.5.4 Curing Conditions

Following compaction, the porous concrete specimens were transferred directly to a temperature-controlled humid curing chamber inside their moulds. In accordance with ASTM C192, the specimens remained in the moulds for 24 hours to achieve initial set. After 24 hours, they had developed sufficient cohesion to be carefully demoulded. The exposed samples were immediately returned to the humid curing chamber to complete the full 7-day moisture curing cycle prior to hardened-state testing.

3.6 Laboratory testing

3.6.1 Porosity

Since the structural and hydraulic performance of porous concrete is governed by its void content, verifying the porosity of each specimen is a necessary step before mechanical testing. The water-displacement procedure developed by Montes et al. (2005), which is based on Archimedes' principle and is consistent with ASTM C1754/C1754M, was used for this purpose.

Subjecting 7-day cured specimens directly to oven temperatures carries the risk of inducing thermal shrinkage and micro-cracking within the young paste. To avoid this, the cylinders were removed from the humid curing chamber on day 6 and placed in a controlled, mild-temperature drying environment for 24 hours to allow internal moisture to evaporate gradually. On day 7, the dry mass (W_d) of each specimen was recorded. The specimens were then fully submerged in a water bath, and their submerged mass (W_s), as shown in Figure 3.10, was recorded following the prescribed submersion period. The total porosity (P) was calculated using the following equation, with the water density (ρ_W) corrected for the measured bath temperature:

$$P = \left(1 - \frac{W_d - W_s}{\rho_W \times V_T}\right) \times 100 \qquad (3.9)$$

where VT is the total bulk volume of the 100×100 mm cylindrical specimen.

Figure 3.10: Submerged weighing of a cured porous concrete specimen to determine its immersed mass (Ws) during porosity validation.

3.6.2 Splitting tensile strength

Indirect (splitting) tensile testing was selected as the primary mechanical indicator rather than compressive testing. Schaefer et al. (2006) established that splitting tensile strength maintains a consistent relationship with compressive strength in porous concrete, generally falling between 12% and 15% of the compressive value. Moreover, Kevern et al. (2009) note that the splitting tensile test accommodates specimens of any diameter and length, whereas compressive testing requires samples with a correct height-to-diameter ratio that SGC-produced cylinders may not satisfy without additional coring. The test was conducted in accordance with ASTM C496/C496M. The aligned specimen placed within the mechanical test device prior to load initialization is pictured in Figure 3.11.

One deliberate deviation from the standard is worth noting. ASTM C496 requires specimens to remain continuously moist until the moment of testing. In this program, the specimens underwent a 24-hour mild drying phase on day 6 followed by submersion for the porosity test on day 7, before a brief period at room temperature prior to loading. This sequence was necessary to establish a direct correlation between the verified void content and the ultimate tensile strength of each individual specimen. Testing the specimens immediately upon exiting the curing chamber would have prevented the porosity measurement, breaking the specimen-specific data pair that the experimental methodology depends on.

Figure 3.11: Indirect tensile strength (ITS) testing of a cured porous concrete specimen on the 7^{th} day of curing.

4. Results

4.1 Aggregate characterisation results

Before evaluating the concrete mixtures, a baseline characterisation of the aggregates was completed to confirm the physical differences between the aggregate shapes and to establish exact inputs for the volumetric mix design equations.

Table 4.1 outlines the pycnometer measurements compiled in accordance with EN 1097-6. All mix design proportions and SSD pre-conditioning quantities reported in this thesis are based exclusively on these measured values.

Table 4.1: Particle density and water absorption of all aggregate fractions, determined by pycnometer in accordance with EN 1097-6

Property	***Risino* (Rounded)**	***Graniglia* (Crushed)**	***Sabbia Fine* (Sand)**
Apparent Particle Density, ρa (Mg/m³)	2.74	2.75	2.74
Oven-Dry Particle Density, ρrd (Mg/m³)	2.68	2.68	2.66
SSD Particle Density, ρssd (Mg/m³)	2.70	2.70	2.69
Water Absorption, WA24 (%)	1.2	1.2	1.4

Table 4.2 presents the geometric shape parameters evaluated in accordance with EN 933-3 and EN 933-4. The *Risino* gravel yields $\text{FI} = 6$ and $\text{SI} = 3$, consistent with the near-spherical geometry expected of naturally water-worn material. The *Graniglia* crushed aggregate yields $\text{FI} = 10$ and $\text{SI} = 14$. The Shape Index value of 14 indicates that 14% by mass of the crushed particles have a length-to-thickness ratio exceeding 3, compared to only 3% for the *Risino*. This geometric elongation, combined with the angular surface texture produced by mechanical fracture, increases the specific surface area of the *Graniglia* skeleton and the inter-particle contact friction that must be overcome during compaction.

Table 4.2: Shape characterisation of coarse aggregate fractions, determined in accordance with BS EN 933-3:2012 (Flakiness Index) and BS EN 933-4:2008 (Shape Index).

Shape Parameter	**Standard**	**Risino (Rounded)**	**Graniglia (Crushed)**
Flakiness Index, FI	EN 933-3	6	10
Shape Index, SI	EN 933-4	3	14

Table 4.3 presents the packing parameters evaluated in accordance with ASTM C29/C29M and EN 1097-3. The compacted void content of the *Risino* is 37.6%, compared to 42.7% for the *Graniglia*, a 5.1 percentage point increase attributable to the angular particles' reduced packing

efficiency under external compaction. The uncompacted contrast is more pronounced: 40.3% for *Risino* versus 48.3% for *Graniglia*, a difference of 8.0 percentage points.

This gap between compacted and uncompacted void content is particularly informative: rounded aggregates, owing to their self-compacting tendency, exhibit an uncompacted void content close to their compacted value, while angular particles naturally resist rearrangement. For the *Risino* this gap is 2.7 percentage points; for the *Graniglia* it is 5.6 percentage points — more than double. This directly confirms the structural consequences of aggregate angularity and provides a physically grounded basis for anticipating the higher CDI values observed for the crushed aggregate mixes.

Table 4.3: Compacted and uncompacted void contents of coarse aggregate fractions, determined in accordance with ASTM C29/C29M and EN 1097-3.

Void Content Parameter	Standard	*Risino* (Rounded)	*Graniglia* (Crushed)
Compacted (Rodded) Void Content (%)	ASTM C29/C29M	37.6	42.7
Uncompacted Void Content (%)	EN 1097-3	40.3	48.3

4.2 Compaction and mechanical test results

Table 4.4 includes the complete experimental dataset. The values represent the calculated means and corresponding standard deviations derived from the laboratory testing of the replicates per mix design.

Table 4.4: Matrix of fresh-state compaction metrics and 7-day mechanical properties.

Mixture	Coarse Aggregate Profile	Binder Ratio (b/a)	Total SGC Gyrations	Workability Energy Index (WEI)	Compaction Densification Index (CDI)	Porosity (%)	Splitting Tensile Strength (MPa)
R24	100% Rounded	24%	9 ± 1	675 ± 0.58	0 ± 1	20.22 ± 0.54	1.56 ± 0.09
R21	100% Rounded	21%	17 ± 2	657 ± 3.00	17 ± 6	20.28 ± 0.26	1.25 ± 0.05
R18	100% Rounded	18%	29 ± 3	637 ± 2.52	80 ± 16	20.86 ± 0.25	1.30 ± 0.10
M24	50/50 Blended	24%	21 ± 3	645 ± 4.36	37 ± 12	20.45 ± 0.32	1.81 ± 0.04
M21	50/50 Blended	21%	34 ± 1	631 ± 5.69	116 ± 15	20.63 ± 0.29	1.56 ± 0.03
M18	50/50 Blended	18%	79 ± 5	609 ± 2.31	501 ± 30	20.71 ± 0.40	1.47 ± 0.15
C24	100% Crushed	24%	52 ± 4	617 ± 6.11	258 ± 45	20.24 ± 0.23	1.67 ± 0.10
C21	100% Crushed	21%	100 ± 5	599 ± 6.11	760 ± 68	19.93 ± 0.31	1.89 ± 0.12
C18	100% Crushed	18%	200 ± 0	580 ± 2.12	1932 ± 3	21.04 ± 0.53	1.81 ± 0.11

Some values in Table 4.4 have specific experimental limitations that affect how they should be understood in the following sections. C18 is the only mix that reached compaction refusal under the 200-gyration protocol, neither specimen achieved the 100 mm target height, reaching around 101.4 mm. Its CDI of 1932 therefore represents a lower bound rather than a true integral to completion, and its porosity and ITS values reflect a slightly more porous, less dense void content than the 20% design target.

4.2.1 Volumetric verification (porosity)

The central principle of this experimental methodology was to maintain the Design Void Content (DVC) at 20% across all nine mixtures. The total porosity of each specimen was verified using the water-displacement procedure established by Montes et al. (2005). The measured porosity results for all nine mix designs are summarised in Figure 4.1.

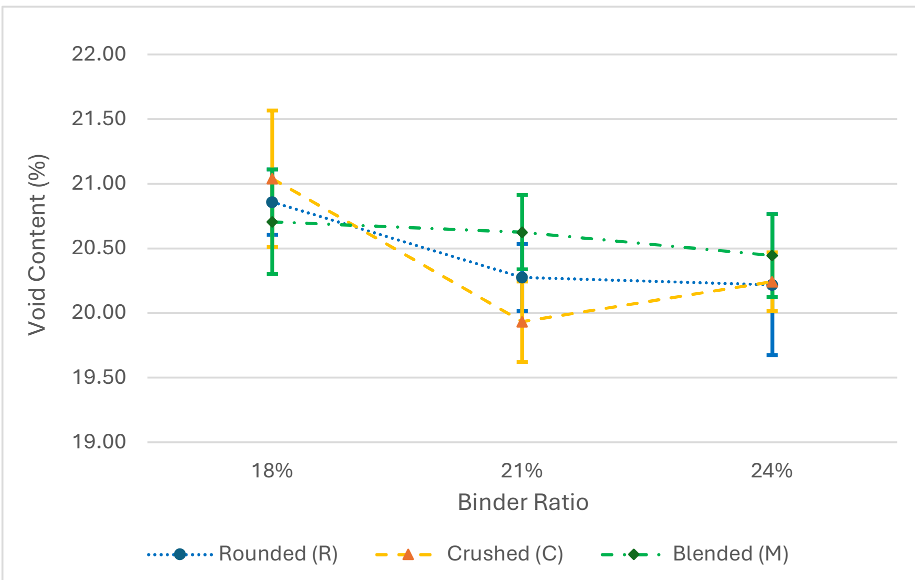

Figure 4.1: Measured porosity of all nine mix designs, with the 20% DVC target indicated.

The porosities remained consistently within the targeted 19.5–21.5% range, confirming the accuracy of the absolute volume mix design equations and the effectiveness of the stop-at-height compaction approach.

4.2.2 WEI and CDI results

The WEI captures the initial flowability and inherent self-compacting tendency of the fresh mixture before significant aggregate interlock develops. A higher WEI indicates a mixture that flows readily into the mould and requires little initial energy to rearrange its particles. The WEI results across all nine mixes are presented in Figure 4.2.

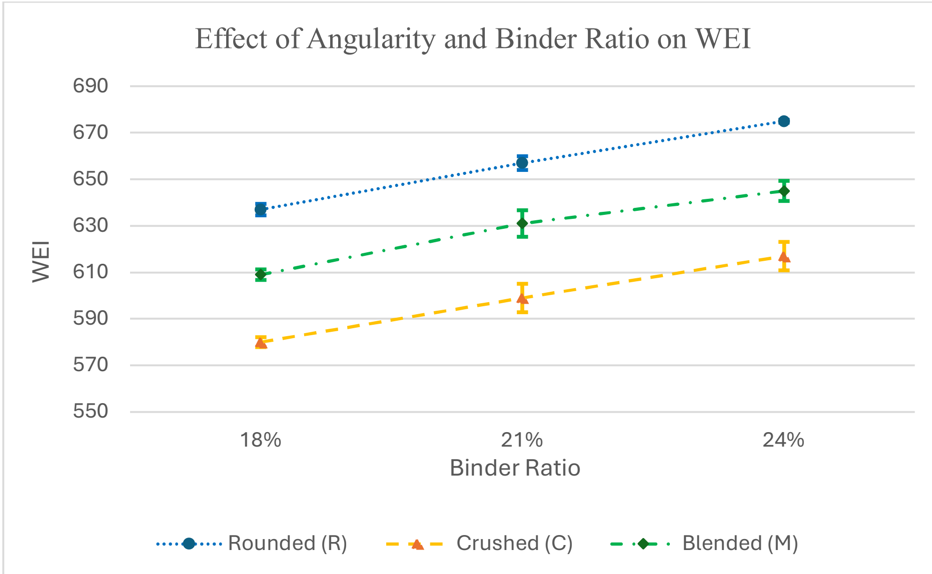

Figure 4.2: Workability Energy Index (WEI) as a function of aggregate type and b/a ratio.

The 100% rounded mixtures consistently recorded the highest WEI values at every paste volume, while the 100% crushed mixtures recorded the lowest WEI values.

While the WEI measures the ease of initial flow, the CDI represents the sustained energy required to densify the mixture from its loose state to the 20% DVC. A lower CDI is operationally desirable, indicating that the mixture reaches its target void content quickly and without requiring more mechanical effort. The CDI results are presented in Figure 4.3.

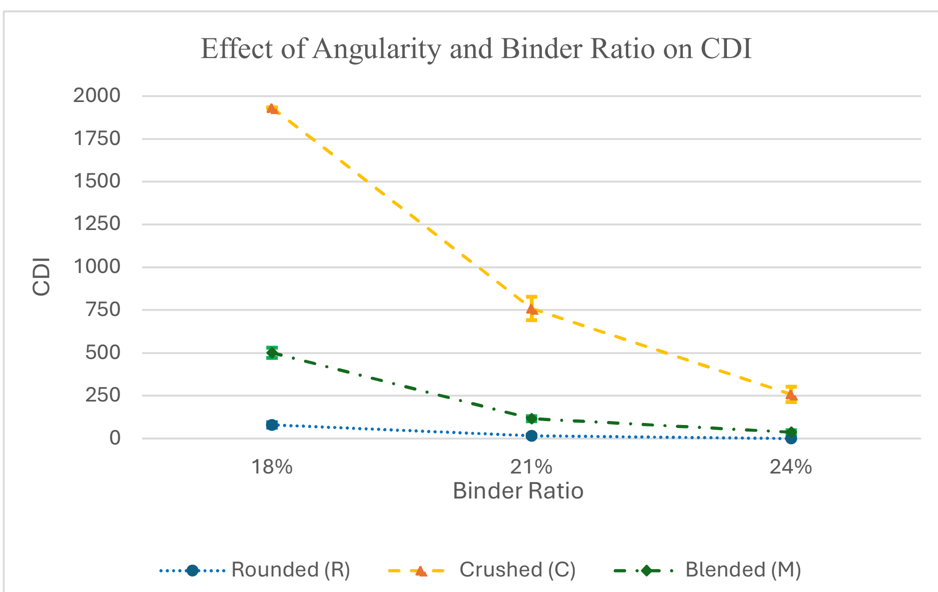

Figure 4.3: Compaction Densification Index (CDI) as a function of aggregate type and b/a ratio.

The contrast between aggregate types is considerable, particularly at the lower paste volumes. The 100% crushed mixtures at 18% b/a required the highest compaction energy recorded in the experimental matrix: the specimens did not reach the 100 mm target height within 200 gyrations, defining a condition of compaction refusal.

4.2.3 Splitting tensile strength results

Following the 7-day curing period, the splitting tensile strength was measured for all 27 specimens (three replicates per mix). The results are presented in Figure 4.4.

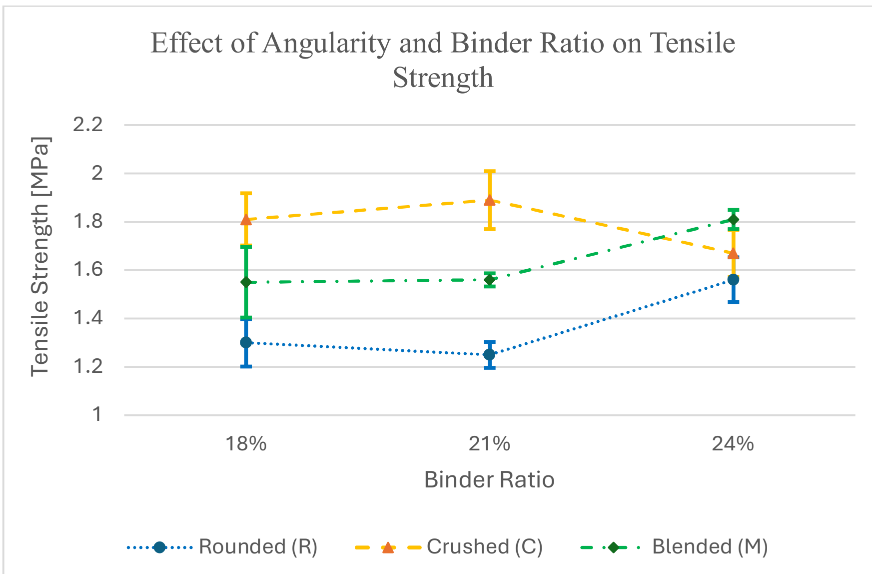

Figure 4.4: Seven-day splitting tensile strength as a function of aggregate type and b/a ratio.

The 100% crushed mixtures recorded the highest tensile strengths across most of the testing matrix. A positive correlation between b/a ratio and tensile strength is evident across all three aggregate profiles.

5. Discussion

5.1 Porosity check

Aggregate type, whether rounded or crushed, had no significant effect on final void content ($p = 0.536$), and the interaction between angularity and paste volume was likewise insignificant ($p = 0.253$) (Table 5.1). Despite the different internal frictions and locking behaviours of the three skeletal profiles, the 200 kPa SGC pressure was sufficient to force every skeleton into its required volumetric content.

Table 5.1: Two-way Analysis of Variance (ANOVA) parameters for the porosity

Source of Variation	Sum of Squares	df	Mean Square	F	p
b-a	1.798	2	0.8992	7.205	**.005**
Aggregate	0.162	2	0.0808	0.648	.536
b-a × Aggregate	0.738	4	0.1845	1.478	.253
Residuals	2.122	17	0.1248	—	—

The slight statistical significance of the b/a ratio on porosity ($p = 0.005$) was isolated entirely to the 18% b/a mixtures, as confirmed by Tukey's post-hoc comparisons (Table 5.2); the porosity difference between the 21% and 24% ratios was negligible ($p = 0.988$). The 18% mixtures, across all three aggregate types, were notably dry and lacked the paste volume needed to adequately coat and separate the particles.

Table 5.2: Tukey's HSD pairwise post-hoc comparisons for binder ratio on porosity

Factor Layer	Pairwise Comparison	Mean Difference	Standard Error (SE)	t-statistic	pTukey
Binder Ratio (b/a)	18% vs. 21%	0.5889	0.173	3.397	**.009**
	18% vs. 24%	0.5644	0.173	3.256	**.012**
	21% vs. 24%	–0.0244	0.167	–0.147	.988

Taken together, the porosity data confirms that volumetric equivalence was achieved across the matrix. Any differences in fresh-state workability indices and hardened mechanical strength reported in the sections below are attributable to the controlled independent variables, aggregate angularity, and b/a ratio, rather than variation in specimen density.

5.2 Discussion of b/a ratio effect

5.2.1 b/a ratio effect on WEI

For the fresh-state parameters, the ANOVA confirmed that both aggregate type and b/a ratio exert a statistically significant effect on the Workability Energy Index (WEI), with $p < 0.001$ for both main effects (Table 5.3). Notably, the interaction between the two variables was not significant for WEI ($p = 0.936$), indicating that paste volume and aggregate morphology influence initial flowability independently and additively, without compounding each other.

Table 5.3: Two-way Analysis of Variance (ANOVA) parameters for the WEI

Source of Variation	Sum of Squares	df	Mean Square	F	p
b-a	5808.8	2	2904.41	165.410	**<.001**
Aggregate	13907.0	2	6953.52	396.013	**<.001**
b-a × Aggregate	13.9	4	3.47	0.197	.936
Residuals	298.5	17	17.56	—	—

To further examine the specific variations caused by the binder content, the main-effects post-hoc comparisons for the binder ratio on WEI are reported in Table 5.4. Every pairwise transition between the binder layers is highly significant ($p < 0.001$), confirming that each step-wise increment in paste volume alters initial flowability in a predictable trend across the matrix.

Table 5.4: Tukey's HSD pairwise post-hoc comparisons for binder ratio on WEI

Factor Layer	Pairwise Comparison	Mean Difference	Standard Error (SE)	t-statistic	pTukey
Binder Ratio (b/a)	18% vs. 21%	–20.7	2.06	–10.08	**<.001**
	18% vs. 24%	–37.4	2.06	–18.19	**<.001**
	21% vs. 24%	–16.7	1.98	–8.44	**<.001**

Increasing the b/a ratio raised the WEI across all three aggregate types. Moving from 18% to 24% provides a thicker paste coating on each particle surface, physically separating the aggregate contacts and reducing the frictional resistance that opposes initial rearrangement. Even for the crushed mixtures, the additional paste at 24% b/a produced a measurable improvement in initial flowability, though these mixes remained well below the rounded equivalents at the same paste volume (Tables 5.4 and B.1.1).

5.2.2 b/a ratio effect on CDI

While the WEI captures initial behavioural features, the sustained energy required to compact the mixture into its final volume is obtained via the CDI. The ANOVA for the CDI indicates both main effects remain highly significant ($p < 0.001$), but the interaction between aggregate type and b/a ratio is also strongly significant ($p < 0.001$) (Table 5.5). This means that the effect of paste volume on compaction resistance depends critically on which aggregate skeleton it is lubricating. This interaction represents a key mechanical relationship investigated in this study.

Table 5.5: Two-way Analysis of Variance (ANOVA) parameters for the CDI

Source of Variation	Sum of Squares	df	Mean Square	F	p
Aggregate	4.13e+6	2	2.07e+6	2159	**<.001**
b-a	2.39e+6	2	1.19e+6	1248	**<.001**
b-a × Aggregate	1.84e+6	4	460029	481	**<.001**
Residuals	16265	17	957	—	—

The main-effects post-hoc comparisons for the single variable of binder ratio on the CDI are presented in Table 5.6. The comparisons show statistical drops in overall compaction energy with each ascending paste tier ($p < 0.001$), highlighting the overarching role of binder content in overcoming aggregate locks.

Table 5.6: Tukey's HSD pairwise post-hoc comparisons for binder ratio on CDI

Factor Layer	Pairwise Comparison	Mean Difference	Standard Error (SE)	t-statistic	pTukey
Binder Ratio (b/a)	18% vs. 21%	540.0	15.2	35.60	**<.001**
	18% vs. 24%	739.0	15.2	48.70	**<.001**
	21% vs. 24%	199.0	14.6	13.70	**<.001**

The CDI data illustrates a clear lubrication threshold. As the b/a ratio increased to 24%, the CDI of the crushed and blended mixtures dropped markedly. The additional paste volume coated the angular particle surfaces, reducing boundary friction sufficiently to allow the skeleton to compact under the applied pressure. This confirms that the compaction resistance of angular aggregates is not an inherent barrier to self-compaction: it can be effectively controlled by defining the paste volume to the correct lubrication threshold for the specific aggregate angularity (Tables 5.6 and B.2.1).

5.2.3 b/a ratio effect on tensile strength

For splitting tensile strength, as presented in Table 5.7, the ANOVA confirmed that both variables significantly affect the tensile strength, though with a clear hierarchy. Aggregate angularity is the dominant factor, with Rounded vs Mixed ($p < 0.001$), Rounded vs Crushed (p

< 0.001), and Mixed vs Crushed (p = 0.012) all returning significant differences. The overall main effect of the b/a ratio is secondary (p = 0.027) and is principally driven by the contrast between the 18% and 24% extremes (p = 0.043), while the 21% vs 24% difference falls just outside significance (p = .053) (Table B.4.1).

Table 5.7: Two-way Analysis of Variance (ANOVA) parameters for the splitting tensile strength

Source of Variation	Sum of Squares	df	Mean Square	F	p
Aggregate	0.7728	2	0.38640	43.78	**<.001**
b-a	0.0799	2	0.03994	4.52	**.027**
b-a × Aggregate	0.2756	4	0.06889	7.81	**<.001**
Residuals	0.1500	17	0.00883	—	—

To isolate how the binder variable behaves independently of aggregate morphology, the main-effects post-hoc comparisons for binder ratio on splitting tensile strength are displayed in Table 5.8. The post-hoc numbers verify that a statistically significant gain in strength occurs only when shifting from 18% to 24% ($p = 0.043$), whereas the 18% vs 21% step displays no significance ($p = 0.977$).

Table 5.8: Tukey's HSD pairwise post-hoc comparisons for binder ratio on splitting tensile strength

Factor Layer	Pairwise Comparison	Mean Difference	Standard Error (SE)	t-statistic	pTukey
Binder Ratio (b/a)	18% vs. 21%	–0.00944	0.0461	–0.21	0.977
	18% vs. 24%	–0.12167	0.0461	–2.64	**0.043**
	21% vs. 24%	–0.11222	0.0443	–2.53	0.053

The analysis also revealed a significant interaction between aggregate type and b/a ratio ($p < 0.001$). At lower paste volumes (18% and 21%), the strength difference between rounded and crushed aggregates is substantial ($p < 0.001$). At the highest paste volume (24%), this difference effectively disappears ($p = 0.831$), indicating that a sufficiently thick paste layer can compensate for the absence of mechanical interlock in smoother aggregate morphologies (Table B.4.1).

The thin paste layer at 18% b/a appears to leave the strength of the matrix almost entirely dependent on the interlock of the aggregate skeleton; because rounded particles offer little geometric interlock, the structural capacity of the R18 mixture is correspondingly low.

5.3 Discussion of aggregate angularity effect

5.3.1 Aggregate angularity effect on WEI

The 100% rounded mixtures consistently recorded the highest WEI values at every paste volume, while the 100% crushed mixtures recorded the lowest values. As previously outlined in the two-way ANOVA parameters (Table 5.3), aggregate angularity exerts a highly significant main effect on initial flowability ($p < 0.001$). To evaluate the specific variations between different morphology independently of paste volume, the main-effects post-hoc comparisons for aggregate shape on WEI are presented in Table 5.9. Every pairwise comparison between the three angularities returns significant results ($p < 0.001$), confirming that each change in aggregate geometry alters the initial particle rearrangement behaviour.

Table 5.9: Tukey's HSD pairwise post-hoc comparisons for aggregate angularity on WEI

Factor Layer	Pairwise Comparison	Mean Difference	Standard Error (SE)	t-statistic	pTukey
Aggregate Angularity	Rounded (R) vs. Crushed (C)	57.8	2.06	28.10	**<.001**
	Rounded (R) vs. Blended (M)	28.2	1.98	14.30	**<.001**
	Blended (M) vs. Crushed (C)	–29.6	2.06	–14.40	**<.001**

The 50/50 blended mixtures demonstrate an intermediate position, showing initial flow features directly between the two angularity boundaries. The post-hoc analysis confirms that the blend achieves an initial workability higher than the crushed stone ($p < 0.001$) yet remains structurally constrained compared to the rounded gravel ($p < 0.001$). This position indicates that during the first eight gyrations—before the aggregate matrix is forced into high-pressure contact—the initial flow of the material is linearly dependent on the proportion of smooth versus fractured surfaces in the mould.

For the crushed mixtures, the additional paste at 24% b/a produced an improvement in initial flowability, though these mixes remained below the rounded equivalents at the same paste volume (Table B.1.1).

5.3.2 Aggregate angularity effect on CDI

The contrast between aggregate types is considerable, particularly at the lower paste volumes. The 100% crushed mixtures at 18% b/a required the highest compaction energy recorded in the experimental matrix, and the specimens did not reach the 100 mm target height within 200 gyrations, defining a condition of compaction refusal.

This behaviour aligns with the two-way ANOVA for the CDI (Table 5.5), where the aggregate main effect is highly significant ($p < 0.001$). To isolate the impact of particle geometry across the entire matrix, the main-effects post-hoc comparisons for aggregate shape on CDI are provided in Table 5.10. The results show statistically significant differences in compaction energy requirements between all mixtures ($p < 0.001$).

Table 5.10: Tukey's HSD pairwise post-hoc comparisons for aggregate angularity on CDI

Factor Layer	Pairwise Comparison	Mean Difference	Standard Error (SE)	t-statistic	pTukey
Aggregate Angularity	Rounded (R) vs. Blended (M)	–185.0	14.6	–12.70	**<.001**
	Rounded (R) vs. Crushed (C)	–951.0	15.2	–62.70	**<.001**
	Blended (M) vs. Crushed (C)	–765.0	15.2	–50.40	**<.001**

This post-hoc data shows the non-linear behaviour of the 50/50 blended mixtures during sustained compaction, where the blend behaves similarly to the rounded gravel. The mean difference between the rounded matrix and the blend is a modest 185.0, whereas the gap between the blend and the pure crushed aggregate increases to 765.0.

The results also confirm that the compaction resistance of angular aggregates can be effectively controlled by defining the paste volume to the correct lubrication threshold for the specific aggregate angularity (Tables 5.6 and B.2.1).

5.3.3 Aggregate angularity effect on tensile strength

Following the 7-day curing period, the splitting tensile strength results established a hierarchy dominated by aggregate angularity, with the 100% crushed mixtures consistently outperforming the rounded mixtures across most of the testing matrix. As noted in the two-way ANOVA parameters (Table 5.7), aggregate angularity represents the primary factor governing the tensile strength ($p < 0.001$).

To evaluate the separate role of particle morphology, the main-effects post-hoc comparisons for aggregate angularity on splitting tensile strength are summarised in Table 5.11. All pairwise transitions return statistically significant differences, demonstrating an increase in splitting tensile capacity as the angularity of the aggregate increases.

Table 5.11: Tukey's HSD pairwise post-hoc comparisons for aggregate shape on splitting tensile strength

Factor Layer	Pairwise Comparison	Mean Difference	Standard Error (SE)	t-statistic	pTukey
Aggregate Angularity	Rounded (R) vs. Blended (M)	–0.27100	0.0443	–6.12	**<.001**
	Rounded (R) vs. Crushed (C)	–0.42200	0.0461	–9.15	**<.001**
	Blended (M) vs. Crushed (C)	–0.15100	0.0461	–3.27	**0.012**

The mechanical capacity of the 50/50 blend displays a non-linear advantage. As shown by the pairwise comparisons, the blended matrix does not experience a drop in strength due to the rounded gravel inclusion; rather, it behaves closely to the crushed aggregate. The strength reduction from the crushed baseline is a minor 0.151 MPa ($p = 0.012$), while it maintains a 0.271 MPa advantage over the rounded matrix ($p < 0.001$). It seems that a 50% fraction of fractured surfaces provides enough mechanical aggregate interlock, without requiring the excessive compaction energy of a pure crushed mixture.

Moreover, the tensile strength of the mixture at 18% b/a appears to be dependent on the interlock of the aggregate skeleton; because rounded particles have low geometric interlock, the structural capacity of the R18 mixture is correspondingly low. At 24% b/a, however, the strength difference between rounded and crushed mixtures becomes statistically negligible ($p = 0.831$) (Table B.4.1), indicating that a sufficiently thick paste layer can compensate for the absence of mechanical interlock in smoother aggregate morphologies.

5.4 Mixture Classification

With the fresh-state and cured-state results established in Section 4.2, the nine mix designs can be organised into a classification framework based on their combined WEI, CDI, and splitting tensile strength. Rather than treating each mix in isolation, grouping them by compaction behaviour reveals the practical field boundaries of the experimental matrix and clarifies where the trade-off between workability and structural capacity is resolvable and where it is not. Table 5.12 summarises the measured indices for all nine mixes alongside their placeability classification and performance verdict.

Table 5.12: Classification and performance of all nine mix designs by WEI, CDI, and 7-day splitting tensile strength.

Mix	Mean WEI	Mean CDI	Mean ITS (MPa)	Classification	Overall Performance
R24	675	0	1.56	Group 1 — Self-Compacting	Acceptable strength; low stability
R21	657	17	1.25	Group 1 — Self-Compacting	High workability; insufficient strength
M24	**645**	**37**	**1.81**	**Group 1 — Self-Compacting**	**The optimal mixture; high workability and strength**
R18	637	80	1.30	Group 2 — Normal Compaction Effort	Low strength; low compaction effort
M21	631	116	1.56	Group 2 — Normal Compaction Effort	Acceptable mechanical and workability balance
C24	617	258	1.67	Group 2 — Normal Compaction Effort	The only acceptable crushed mixture
M18	609	501	1.47	Group 3 — Considerable Effort	Paste-starved; loss of aggregates lubrication
C21	599	760	1.89	Group 3 — Considerable Effort	Maximum interlock; high compaction effort
C18	580	1932	1.81	Group 3 — Refusal	Compaction refusal

5.4.1 Group 1 — *Self-Compacting Mixtures (CDI ≤ 50)*

Three mixes achieved a self-compacting state under 200 kPa compaction: R24 (CDI = 0), R21 (CDI = 17), and M24 (CDI = 37). In all three cases, the paste volume was sufficient to promote the aggregate particles rearrangement during compaction, and the SGC reached the 100 mm target height with negligible resistance.

R24 and R21 reached this state through the intrinsic low friction of the rounded aggregate skeleton. R24 recorded the highest WEI in the matrix (675) and a CDI of zero, meaning the specimen reached its design void content within the first eight gyrations without requiring any additional densification energy. However, due to the smooth particle rearrangement and limited aggregate surface adhesion, R24 achieves an average tensile strength of only 1.56 MPa. R21 follows the same pattern at a slightly lower paste volume, with a CDI of 17 and an average tensile strength of 1.25 MPa — the lowest recorded in the matrix.

The M24 mixture is characterised by a CDI of 37, reflecting the residual friction introduced by the 50% crushed fraction, but it remains within the self-compacting threshold. Unlike the purely rounded mixtures in this group, M24 maintained a high average splitting tensile strength of 1.81 MPa. Because M24 is the only design in Group 1 that successfully combines self-compacting placement with high structural capacity, it is identified as the optimal mixture of this study and is discussed in detail within Section 5.5.

5.4.2 Group 2 — *Normal Compaction Effort Mixtures (50 < CDI ≤ 300)*

Three mixes fall within a range of moderate, practical compaction resistance: R18 (CDI = 80), M21 (CDI = 116), and C24 (CDI = 258). These mixes require sustained but manageable compaction energy to reach the design void content, and all three are in principle placeable in the field with conventional mechanised equipment, though none achieves self-compaction.

R18 possesses the lower boundary of this group with a CDI of 80. Its WEI of 637 reflects adequate initial flowability, but at 18% b/a, the paste is insufficient to fully coat the rounded aggregates, and the mean tensile strength drops to 1.30 MPa — indicating paste starvation at the aggregate contacts rather than a structural failure of the paste itself.

M21 represents the most balanced mixture in Group 2, with a CDI of 116 and an average tensile strength of 1.56 MPa. Neither index is exceptional, but neither is problematic: the blended skeleton at 21% paste produces a mix that is predictable and consistently placeable. It is the closest equivalent to a conventional industry compromise — adequate on both dimensions without excelling on either.

C24 is the only purely crushed mixture within Group 2. The 24% paste volume reduces the CDI of the crushed aggregate skeleton from unworkable values (CDI = 760 at 21% b/a) to 258, demonstrating the scale of the lubrication effect that the additional paste provides. However, the thicker paste layer might physically separate the angular particles further than at lower b/a ratios, potentially reducing the aggregate-to-aggregate contact. This could explain why the mean tensile strength of C24 (1.67 MPa) is lower than that of C21 (1.89 MPa). The C21 mixture may achieve a greater aggregate interlock because a thinner paste layer at 21% b/a potentially allows the angular particles to remain in closer proximity. C24 is therefore the only crushed mix that is practically placeable.

5.4.3 Group 3 — *Considerable Effort and Refusal Mixtures (CDI > 300)*

The remaining three mixes required compaction energy that would be impractical to replicate in field conditions: M18 (CDI = 501), C21 (CDI = 760), and C18 (CDI = 1932).

For M18, which has a CDI of 501, despite the lubrication benefit of the 50% rounded fraction, the paste volume appears to be insufficient to adequately coat the angular contacts of the blended skeleton under 200 kPa. The result is a mix that requires prolonged compaction energy with limited strength — an average tensile strength of 1.47 MPa that falls below both M21 and M24, confirming that paste starvation in the blended mixture reduces mechanical performance alongside workability.

C21 recorded a CDI of 760, the highest workable value in the matrix, alongside the highest mean splitting tensile strength of 1.89 MPa. Maximum mechanical interlock was achieved when the 21% paste layer was sufficiently thin to allow close angular-to-angular particle contact, resulting in compaction resistance that no slipform paver could realistically sustain. C21 achieved the highest mechanical performance in this experimental matrix, but it is not a viable mixture for field application.

C18 represents a complete placement failure. With a CDI of 1932 and a WEI of 580, the 18% paste volume provides no lubrication for the fully crushed angular skeleton under 200 kPa. The SGC was unable to compact this mixture to the 100 mm target height within 200 gyrations, a condition of compaction refusal. This result defines the hard lower boundary of the experimental layout: below a certain paste volume, a fully crushed aggregate skeleton under high-energy mechanised compaction is an engineering constraint.

The three-group classification confirms that the self-compacting threshold is accessible for blended and rounded aggregates at sufficient paste volumes but is structurally unacceptable for purely rounded systems and physically unachievable for fully crushed aggregates at low paste volumes. This classification establishes the basis for identifying the M24 mix design as the optimal mixture of this study in Section 5.5.

5.5 Identification of the Optimal Self-Compacting Mixture

The objective of this research was to identify a mix design that simultaneously achieves a self-compacting fresh state suitable for slipform paving and a mechanical strength adequate for low traffic loads. As classified and compared in Table 5.12, the experimental results define two opposing extremes within the experimental matrix.

The 100% rounded mixtures (R18, R21, R24) consistently produced the lowest compaction resistance and the highest initial flowability. Their CDI values indicate that these mixes would consolidate under mechanised placement with minimal energy. However, the same smooth morphology that reduces compaction resistance also limits tensile strength: the absence of angularity and aggregate interlock produces the lowest tensile strengths in the matrix.

The 100% crushed mixtures at 18% and 21% b/a (C18, C21) are in the opposite extreme: the angular mixture produces high mechanical interlock and the highest tensile strengths, but the internal friction of the crushed particles at low paste volumes produces CDI values far too high for viable field placement.

The M24 mixture (Figure 5.1), a 50/50 blend of rounded and crushed aggregates at a 24% b/a ratio, has the most favourable position in this mix design, combining a low CDI with a mean tensile strength of 1.81 MPa. The physical basis for this performance might be in how the blended aggregate skeleton, and the 24% paste volume interact under 200 kPa compaction.

Figure 5.1: The M24 mix design in its fresh and cured states

Compared with the fully crushed mixtures, the blended aggregate skeleton reduced internal friction during compaction. The rounded particles likely interrupted direct angular-to-angular contacts, lowering the resistance to particle rearrangement and reducing the CDI to a level compatible with mechanised placement. At the same time, the crushed aggregate provided sufficient angular surface area to increase mechanical interlock, which may explain why the mixture retained a considerably higher tensile strength than the purely rounded mixtures.

The 24% paste volume further contributed to this behaviour. At this b/a ratio, the paste was likely sufficient to coat the angular aggregate surfaces and fill the voids within the blended skeleton, contributing to the reduction in CDI observed relative to the M18 and M21 mixtures. The same paste volume may also have provided adequate bonding between particles, compensating for the smoother surface texture of the rounded aggregate and allowing the mixture to achieve a mean splitting tensile strength of 1.81 MPa. This interpretation is supported by the statistical analysis, which showed that the difference in tensile strength between aggregate angularities was no longer significant at a 24% b/a ratio ($p = 0.831$) (Table B.4.1).

Taken together, these findings suggest that neither aggregate morphology nor paste volume alone controls mixture performance. Increasing the paste volume in the fully crushed mixture (C24) produced a tensile strength comparable to that of M24, although its CDI remained higher, possibly because of the greater friction associated with the fully angular aggregate mixture. Conversely, the blended aggregate skeleton in M18 reduced compaction resistance but did not provide sufficient paste to develop comparable tensile strength. The results therefore suggest that the combination of a 50/50 aggregate blend and a 24% paste volume provides a favourable balance between workability and mechanical performance under 200 kPa compaction. More broadly, these findings indicate that, for heavy-duty mechanised placement of porous concrete, aggregate morphology and paste volume are likely to be most effective when considered together during mixture design rather than optimised independently.

6. Conclusions

This experimental research investigates a porous concrete mixtures optimised for heavy-duty mechanised placement, such as slipform paving. By analysing the interactive mechanics between coarse aggregate angularity (rounded, crushed, and blended) and the cementitious paste volume (18%, 21%, and 24% binder-to-aggregate ratios) under a compaction pressure of 200 kPa, this study identified the thresholds required to balance self-compacting behaviour with mechanical strength.

Based on the laboratory testing program, the following principal conclusions are drawn:

1. Validation of the constant-volume compaction methodology

The utilisation of the constant-volume "stop-at-height" Superpave Gyratory Compactor methodology proved to be effective for porous concrete mixtures. By calculating the exact absolute constituent volumes and targeting the 100 mm compacted height, the design void content was held at approximately 20% across the experimental matrix, verified using the Montes et al. (2005) water-displacement method. One exception was C18, the fully crushed mixture at the lowest paste content, which reached compaction refusal under the full 200-gyration protocol without reaching the 100 mm target height, resulting in a slightly higher porosity than the rest of the matrix.

Statistical analysis confirmed that neither the aggregate type nor the interaction of variables significantly affected the porosity, thus demonstrating the effectiveness of the initial mix-design calculations. This allowed to isolate the effects of the independent variables (i.e., aggregate angularity and b/a ratio) on the strength and compaction parameters.

2. Compaction parameters

The fresh-state compaction metrics — the Workability Energy Index (WEI) and Compaction Densification Index (CDI) — showed that aggregate morphology and paste volume cause competing effects during placement. Mixtures comprising 100% rounded river gravel exhibited high initial flowability (WEI) and required minimal compaction energy (CDI), consistent with the low interparticle friction of smooth, rounded particles. The 100% crushed aggregate mixtures, by contrast, generated higher internal friction and resisted compaction. this eased considerably with more paste by raising b/a ratio to 24%, but even at this level, the fully crushed mixture did not reach a self-compacting state.

The 50/50 blended mixtures, however, did not sit midway between the two extremes: across all three paste volumes, their CDI were closer to the rounded mixtures than to the crushed ones, showing that half fraction of the rounded aggregate is sufficient to bring the blended mixture's compaction behaviour close to that of a fully rounded one.

3. Mechanical properties

Aggregate angularity was the dominant factor controlling splitting tensile strength, with the crushed mixtures outperforming the rounded mixtures. The b/a ratio played a secondary role, and its influence depended on the aggregate morphology. At the lower b/a ratios, the gap between rounded and crushed aggregate was wide, but this gap narrowed considerably at the higher paste volume.

Moreover, the tensile strength of the blended mixtures rose as paste content increased, to the point where, at the 24% b/a ratio, the 50/50 blend exceeded the fully crushed mixture. This indicates that a 50% fraction of crushed aggregate is sufficient to provide the interlock needed for strength, without increasing the compaction effort of a fully crushed mixture.

4. Optimal Mixture

Comparing the fresh-state compaction indices (WEI and CDI) against the splitting tensile strength identified the M24 mix — a 50/50 mass blend of rounded and crushed aggregates at a 24% b/a ratio — as the optimal mixture.

The M24 mixture resolves the conflict identified in Point 2 above. Its fresh-state behaviour is close to that of the rounded mixtures, since the rounded fraction lowers the overall internal friction of the blended skeleton, while the retained crushed fraction preserves the mechanical interlock needed to maintain mechanical performance. At a 24% b/a ratio, the paste volume is sufficient to bring this blended mixture to a self-compacting state under 200 kPa. The M24 mixture therefore emerges as the optimal design in the experimental matrix, achieving self-compacting behaviour without compromising mechanical performance, and retaining an average 7-day splitting tensile strength of 1.81 MPa.

6.1 Limitations and recommendations for future research

The findings of this study are subject to several limitations that should inform future work. First, the mechanical performance was evaluated at 7 days only. While this reflects field opening conditions as documented by Kevern et al. (2009), the long-term strength development and durability, including freeze-thaw resistance, abrasion, and permeability retention over time, remain uncharacterised. A 28-day and long-term testing program would strengthen the case for structural deployment.

Second, the compaction indices derived in this study use a height-ratio integration under 200 kPa and are therefore not directly comparable to the numerical thresholds established by Kevern et al. (2009) at 60 kPa. Establishing calibrated WEI and CDI classification thresholds specific to 200 kPa compaction and height-based integration is a necessary step before these indices can be used as standardised acceptance criteria for slipform paving operations.

Third, all aggregates were sourced from a single quarry in Carignano, Turin, sharing a uniform mineralogical profile. The influence of lithological variation — softer limestones, higher-absorption volcanic aggregates, or materials with different surface energy characteristics — on the optimal b/a ratio and the ITZ failure transition remains unknown. Replicating this experimental matrix with aggregates from different geological sources would establish the generalisability of the design principle.

Finally, this study evaluated only one type of cement. The incorporation of supplementary cementitious materials such as fly ash or ground granulated blast-furnace slag, which alter paste viscosity and ITZ chemistry, could change the lubrication threshold and the optimal b/a ratio. Investigating these combinations within the same volumetrically controlled framework would extend the practical applicability of the findings to more sustainable mix designs.

References

Standards and Technical Guidelines

ACI Committee 522. (2006). Pervious Concrete (ACI 522R-06). American Concrete Institute, Farmington Hills, MI.

Asphalt Institute. (2001). Superpave Mix Design. Superpave Series No. 2 (SP-2). Asphalt Institute, Lexington, KY.

ASTM C192/C192M. Standard Practice for Making and Curing Concrete Test Specimens in the Laboratory. ASTM International, West Conshohocken, PA.

ASTM C496/C496M. Standard Test Method for Splitting Tensile Strength of Cylindrical Concrete Specimens. ASTM International, West Conshohocken, PA.

ASTM C1754/C1754M-25. Standard Test Method for Density and Void Content of Hardened Pervious Concrete. ASTM International, West Conshohocken, PA.

ASTM C29/C29M. Standard Test Method for Bulk Density ("Unit Weight") and Voids in Aggregate. ASTM International, West Conshohocken, PA..

BS EN 932-2:1999. Tests for General Properties of Aggregates — Part 2: Methods for Reducing Laboratory Samples. British Standards Institution, London.

BS EN 933-3:2012. Tests for Geometrical Properties of Aggregates — Part 3: Determination of Particle Shape — Flakiness Index. British Standards Institution, London.

BS EN 933-4:2008. Tests for Geometrical Properties of Aggregates — Part 4: Determination of Particle Shape — Shape Index. British Standards Institution, London.

BS EN 1097-3:1998. Tests for Mechanical and Physical Properties of Aggregates — Part 3: Determination of Loose Bulk Density and Voids. British Standards Institution, London.

BS EN 1097-6:2013. Tests for Mechanical and Physical Properties of Aggregates — Part 6: Determination of Particle Density and Water Absorption. British Standards Institution, London.

EN 197-1:2011. Cement — Part 1: Composition, Specifications and Conformity Criteria for Common Cements. European Committee for Standardisation (CEN), Brussels.

UNI 8520-22:2020. Aggregati per Calcestruzzo — Parte 22: Valutazione della Reattività Alcali-Silice. Ente Nazionale Italiano di Unificazione (UNI), Milan.

UNI EN 12620:2008. Aggregati per Calcestruzzo. Ente Nazionale Italiano di Unificazione (UNI), Milan.

UNI EN 13139:2003. Aggregati per Malta. Ente Nazionale Italiano di Unificazione (UNI), Milan.

Books, Reports and Dissertations

Kevern, J. T. (2008). Advancements in Pervious Concrete Technology. Ph.D. Dissertation, Iowa State University, Ames, IA.

Nassiri, S., Rangelov, M., and Chen, Z. (2017). Preliminary Study to Develop Standard Acceptance Tests for Pervious Concrete. Report No. WA-RD 868.1, Washington State Department of Transportation, Olympia, WA.

Schaefer, V. R., Wang, K., Suleiman, M. T., and Kevern, J. T. (2006). Mix Design Development for Pervious Concrete in Cold Weather Climates. Report prepared for the National Concrete Pavement Technology Center, Iowa State University, Ames, IA.

Tennis, P. D., Leming, M. L., and Akers, D. J. (2004). Pervious Concrete Pavements. EB302, Portland Cement Association (PCA) and National Ready Mixed Concrete Association (NRMCA), Skokie, IL.

Journal Articles

Adresi, M., Yamani, A., Karimaei Tabarestani, M., and Rooholamini, H. (2023). A comprehensive review on pervious concrete. Construction and Building Materials, 407, 133308.

Bassani, M., Tefa, L., Sabia, D., and Palmero, P. (2022). Optimal constituent mix ratio for improved fresh properties of cementitious and alkali-activated porous concretes. Journal of Materials in Civil Engineering, 34(11), 04022308.

Chandrappa, A. K., and Biligiri, K. P. (2016). Pervious concrete as a sustainable pavement material — Research findings and future prospects: A state-of-the-art review. Construction and Building Materials, 111, 262–274.

Chen, Y., Wang, K., Wang, X., and Zhou, W. (2013). Strength, fracture and fatigue of pervious concrete. Construction and Building Materials, 42, 97–104.

Chinchillas-Chinchillas, M. J., et al. (2014). Influence of the shape of natural aggregates, recycled and silica fume on the mechanical properties of pervious concrete. International Journal of Advanced Computer Science and Its Applications, 4(4), 216–220.

Chockalingam, T., Vijayaprabha, C., and Leon Raj, J. (2023). Experimental study on size of aggregates, size and shape of specimens on strength characteristics of pervious concrete. Construction and Building Materials, 385, 131320.

Elango, K. S., and Revathi, V. (2017). Fal-G binder pervious concrete. Construction and Building Materials, 140, 91–99.

Ibrahim, A., Mahmoud, E., Yamin, M., and Patibandla, V. C. (2014). Experimental study on Portland cement pervious concrete mechanical and hydrological properties. Construction and Building Materials, 50, 524–529.

Jain, A. K., and Chouhan, J. S. (2011). Effect of shape of aggregate on compressive strength and permeability properties of pervious concrete. International Journal of Advanced Engineering Research and Studies, 1(1), 120–126.

Kevern, J. T., Schaefer, V. R., and Wang, K. (2009). Evaluation of pervious concrete workability using gyratory compaction. Journal of Materials in Civil Engineering (ASCE), 21(12), 764–770.

Montes, F., Valavala, S., and Haselbach, L. M. (2005). A new test method for porosity measurements of Portland cement pervious concrete. Journal of ASTM International, 2(1), 1–13.

Mrakovčić, S., Čeh, N., and Jugovac, V. (2014). Effect of aggregate grading on pervious concrete properties. Građevinar, 66(2), 107–113.

Nguyen, D. H., Sebaibi, N., Boutouil, M., Leleyter, L., and Baraud, F. (2014). A modified method for the design of pervious concrete mix. Construction and Building Materials, 73, 271–282.

Yu, F., Sun, D., Wang, J., and Hu, M. (2019). Influence of aggregate size on compressive strength of pervious concrete. *Construction and Building Materials*, 209, 463–475.

Wang, J., et al. (2022). Effects of porous pavements on urban heat island mitigation and stormwater runoff control. [As compiled in Adresi et al., 2023.]

Xu, M., et al. (2018). Comprehensive operational framework and blue-green infrastructure components of the Sponge City concept. [As compiled in Adresi et al., 2023.]

Appendix A: Gyratory compaction curves

This appendix presents the complete set of compaction curves recorded by the Superpave Gyratory Compactor for all twenty-seven specimens produced in this experimental campaign (three replicates per each mixture design).

To evaluate the repeatability and homogeneity of each mixture, the compaction progression is reported as one comprehensive graph per mixture design group, with the three replicate curves plotted together. In accordance with the methodology established in Section 3.5.3, the ordinate displays the dimensionless Degree of Compaction ($C(N)$, %) derived from continuous specimen height tracking , plotted against the abscissa representing the gyration count (N) on a linear scale.

Each graph ends when the specimens reach the 100 mm target height (representing the 20% Design Void Content), with the exception of the C18 mixture, which represents compaction refusal and is plotted up to the maximum machine threshold of 200 gyrations.

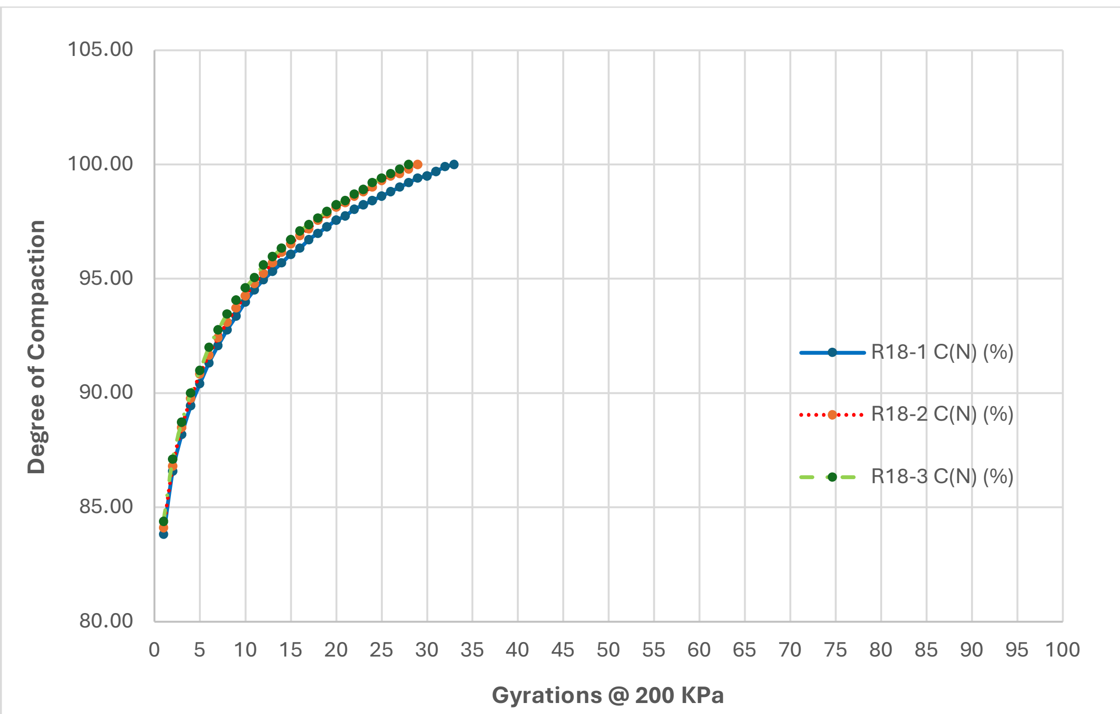

Figure A.1: Compaction curves for the R18 mixture replicates (R18-1, R18-2, R18-3)

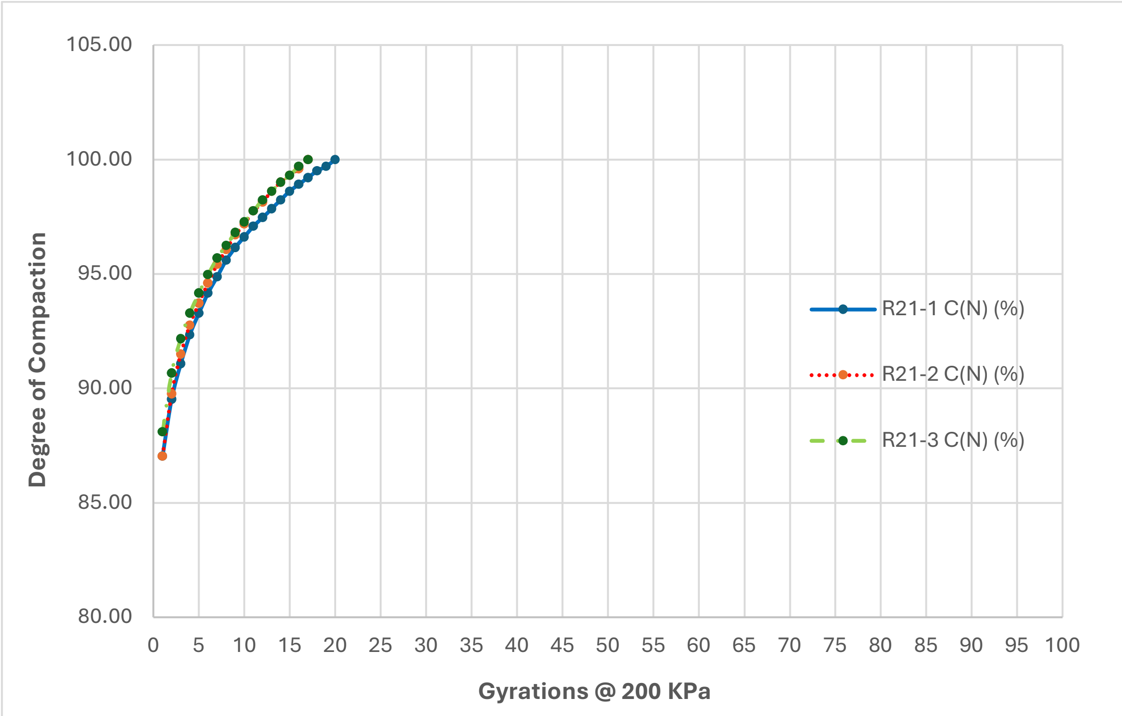

Figure A.2: Compaction curves for the R21 mixture replicates (R21-1, R21-2, R21-3)

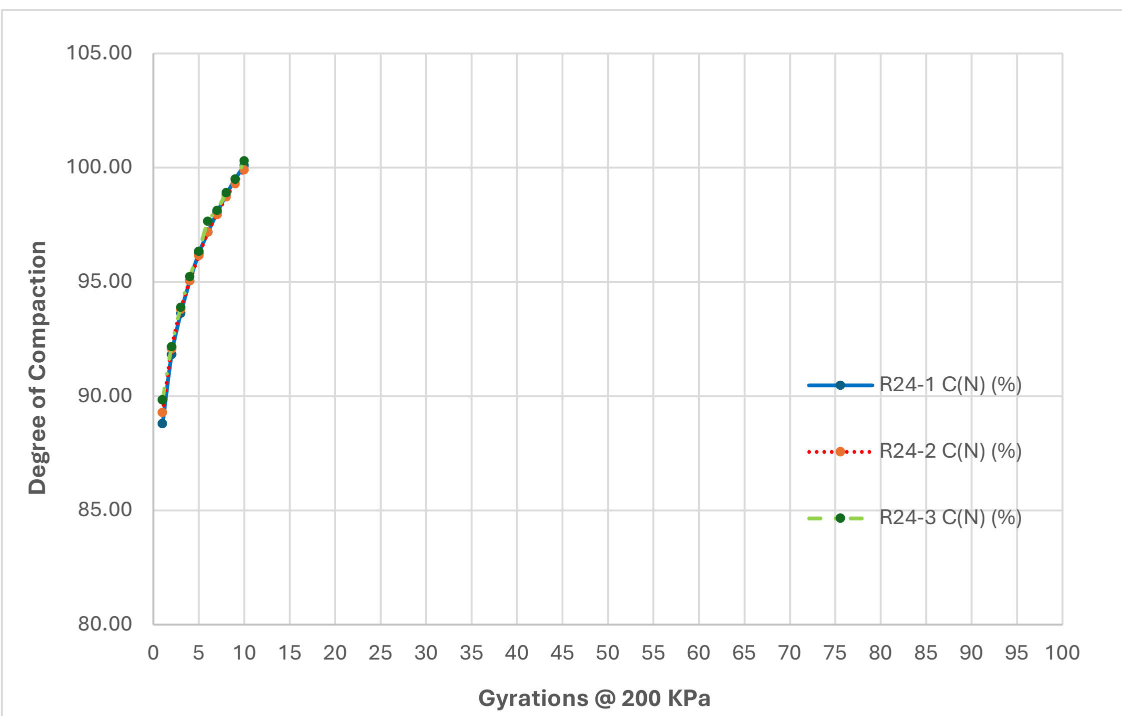

Figure A.3: Compaction curves for the R24 mixture replicates (R24-1, R24-2, R24-3)

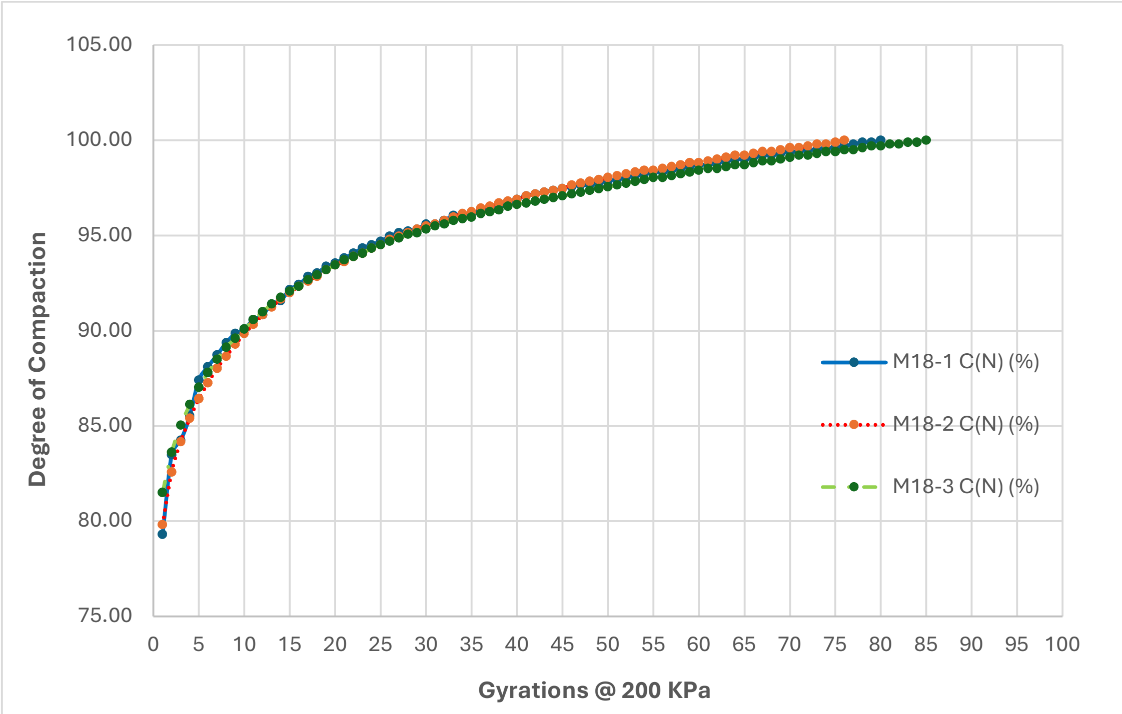

Figure A.4: Compaction curves for the M18 mixture replicates (M18-1, M18-2, M18-3)

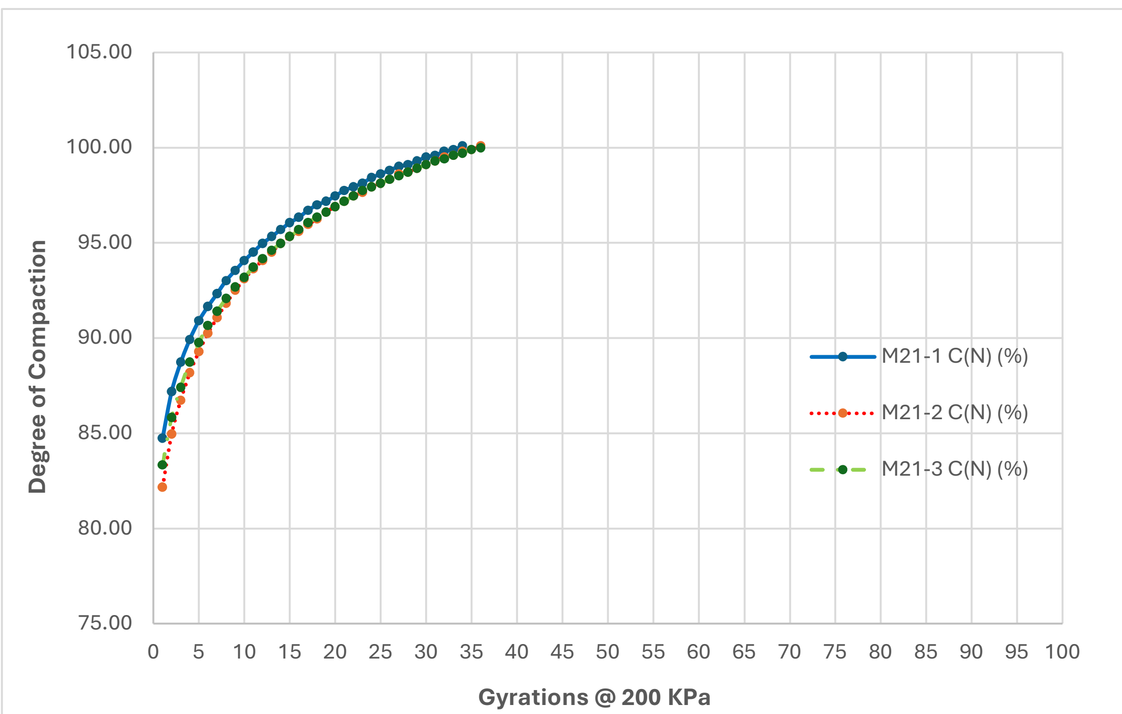

Figure A.5: Compaction curves for the M21 mixture replicates (M21-1, M21-2, M21-3)

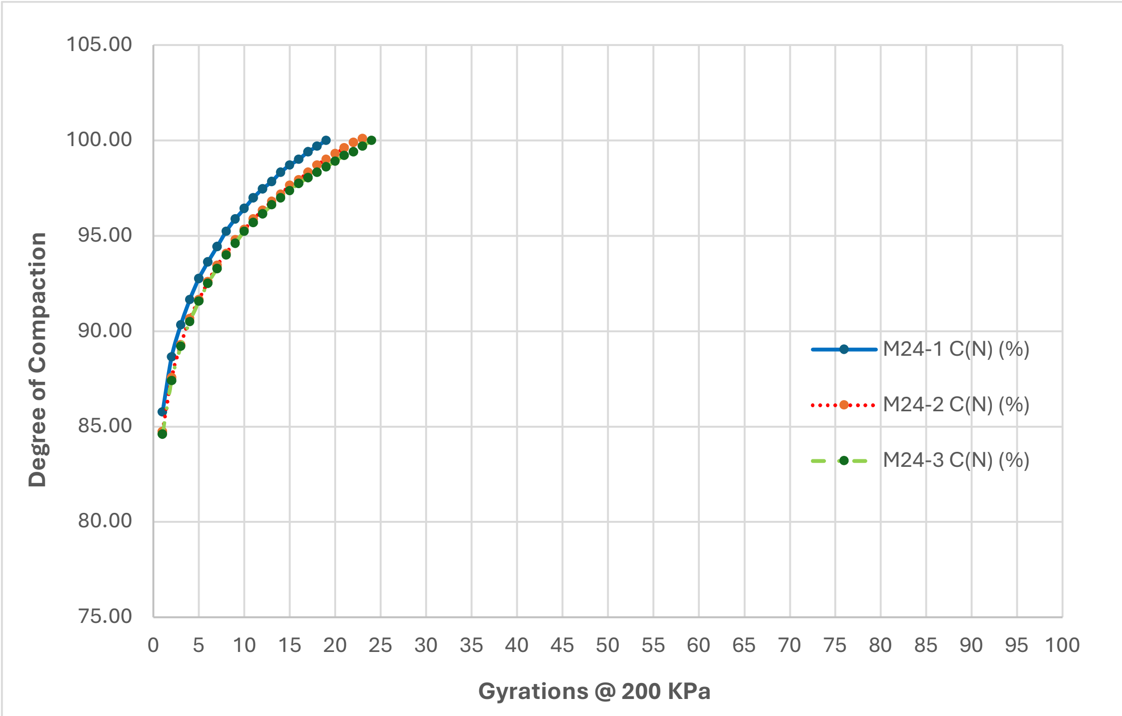

Figure A.6: Compaction curves for the M24 mixture replicates (M24-1, M24-2, M24-3)

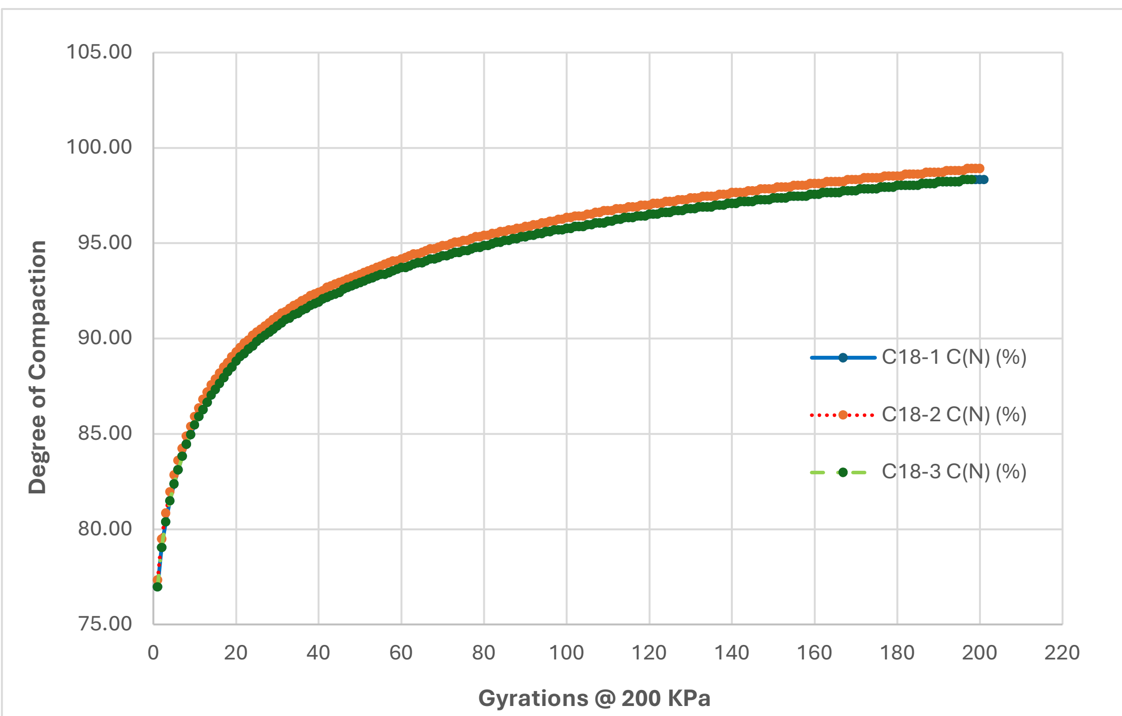

Figure A.7: Compaction curves for the C18 mixture replicates (C18-1, C18-2, C18-3)

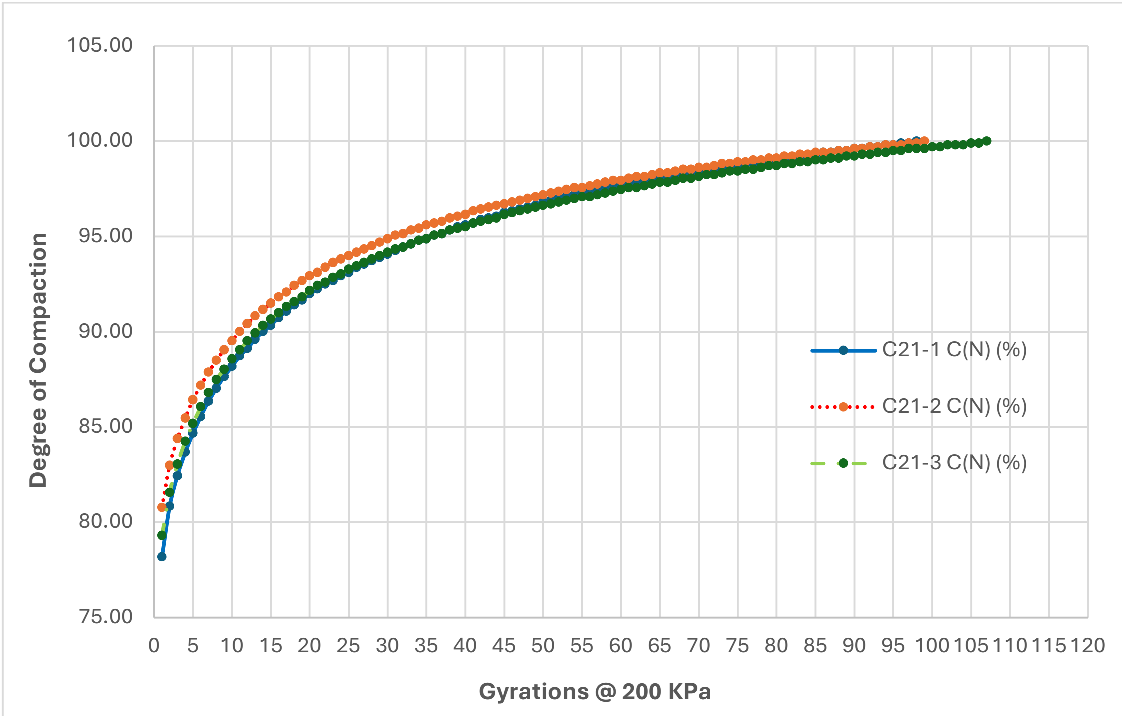

Figure A.8: Compaction curves for the C21 mixture replicates (C21-1, C21-2, C21-3)

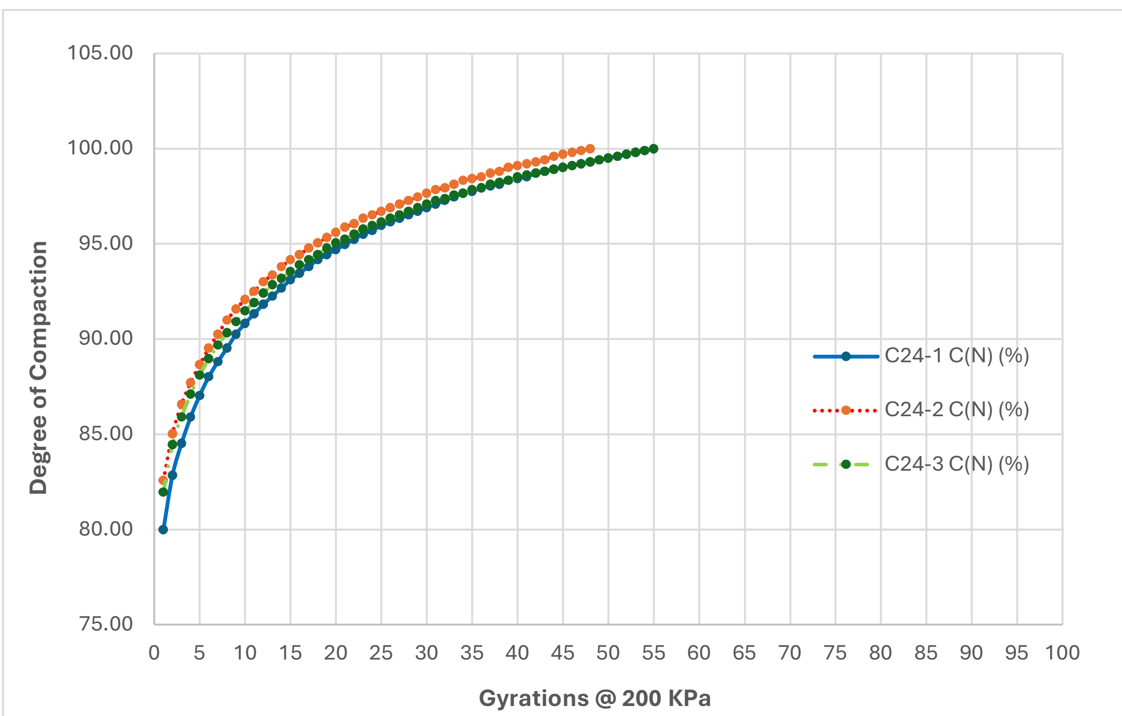

Figure A.9: Compaction curves for the C24 mixture replicates (C24-1, C24-2, C24-3)

Appendix B: Post-Hoc Comparisons (Tukey's HSD)

This appendix provides the comprehensive post-hoc pairwise comparison tables generated using Tukey's Honestly Significant Difference (HSD) test following the two-way Analysis of Variance (ANOVA) detailed in Section 5. The significance threshold was maintained at $\alpha = 0.05$. Comparisons where $p < 0.05$ are shown in bold.

B.1 Fresh-State Workability Energy Index (WEI)

Table B.1.1 gives the full pairwise interaction matrix across all nine mix designs for WEI.

Table B.1.1: WEI Full Interaction Matrix (b/a × Aggregate)

Baseline Combination	vs.	Comparison Combination	Mean Difference	Standard Error (SE)	t-statistic	pTukey
18% Binder Ratio						
18% Rounded (R)	vs.	18% Crushed (C)	57.17	3.83	14.94	**< .001**
	vs.	18% Blended (M)	28.00	3.42	8.18	**< .001**
	vs.	21% Rounded (R)	–20.33	3.42	–5.94	**< .001**
	vs.	21% Crushed (C)	37.33	3.42	10.91	**< .001**
	vs.	21% Blended (M)	6.00	3.42	1.75	.709
	vs.	24% Rounded (R)	–38.67	3.42	–11.30	**< .001**
	vs.	24% Crushed (C)	20.00	3.42	5.85	**< .001**
	vs.	24% Blended (M)	–8.33	3.42	–2.44	.326
18% Crushed (C)	vs.	18% Blended (M)	–29.17	3.83	–7.62	**< .001**

	vs.	21% Rounded (R)	–77.50	3.83	–20.26	**< .001**
	vs.	21% Crushed (C)	–19.83	3.83	–5.18	**.002**
	vs.	21% Blended (M)	–51.17	3.83	–13.38	**< .001**
	vs.	24% Rounded (R)	–95.83	3.83	–25.05	**< .001**
	vs.	24% Crushed (C)	–37.17	3.83	–9.72	**< .001**
	vs.	24% Blended (M)	–65.50	3.83	–17.12	**< .001**
18% Blended (M)	vs.	21% Rounded (R)	–48.33	3.42	–14.13	**< .001**
	vs.	21% Crushed (C)	9.33	3.42	2.73	.209
	vs.	21% Blended (M)	–22.00	3.42	–6.43	**< .001**
	vs.	24% Rounded (R)	–66.67	3.42	–19.49	**< .001**
	vs.	24% Crushed (C)	–8.00	3.42	–2.34	.373
	vs.	24% Blended (M)	–36.33	3.42	–10.62	**< .001**
21% Binder Ratio						
21% Rounded (R)	vs.	21% Crushed (C)	57.67	3.42	16.85	**< .001**
	vs.	21% Blended (M)	26.33	3.42	7.70	**< .001**
	vs.	24% Rounded (R)	–18.33	3.42	–5.36	**.001**
	vs.	24% Crushed (C)	40.33	3.42	11.79	**< .001**

	vs.	24% Blended (M)	12.00	3.42	3.51	.052
21% Crushed (C)	vs.	21% Blended (M)	–31.33	3.42	–9.16	**< .001**
	vs.	24% Rounded (R)	–76.00	3.42	–22.21	**< .001**
	vs.	24% Crushed (C)	–17.33	3.42	–5.07	**.002**
	vs.	24% Blended (M)	–45.67	3.42	–13.35	**< .001**
21% Blended (M)	vs.	24% Rounded (R)	–44.67	3.42	–13.06	**< .001**
	vs.	24% Crushed (C)	14.00	3.42	4.09	**.017**
	vs.	24% Blended (M)	–14.33	3.42	–4.19	**.014**
24% Binder Ratio						
24% Rounded (R)	vs.	24% Crushed (C)	58.67	3.42	17.15	**< .001**
	vs.	24% Blended (M)	30.33	3.42	8.87	**< .001**
24% Crushed (C)	vs.	24% Blended (M)	–28.33	3.42	–8.28	**< .001**

B.2 Fresh-State Compaction Densification Index (CDI)

Table B.2.1 presents the full pairwise interaction matrix across all nine mix designs for CDI.

Table B.2.1: CDI Full Interaction Matrix (Aggregate × b/a)

Baseline Combination	vs.	Comparison Combination	Mean Difference	Standard Error (SE)	t-statistic	pTukey

Rounded Matrix (R)						
Rounded (18%)	vs.	Rounded (21%)	62.7	25.3	2.481	.305
	vs.	Rounded (24%)	79.7	25.3	3.154	.100
	vs.	Blended (18%)	–421.3	25.3	–16.683	**< .001**
	vs.	Blended (21%)	–35.7	25.3	–1.412	.878
	vs.	Blended (24%)	43.0	25.3	1.703	.738
	vs.	Crushed (18%)	–1852.0	28.2	–65.588	**< .001**
	vs.	Crushed (21%)	–680.3	25.3	–26.938	**< .001**
	vs.	Crushed (24%)	–178.0	25.3	–7.048	**< .001**
Rounded (21%)	vs.	Rounded (24%)	17.0	25.3	0.673	.999
	vs.	Blended (18%)	–484.0	25.3	–19.164	**< .001**
	vs.	Blended (21%)	–98.3	25.3	–3.893	**.025**
	vs.	Blended (24%)	–19.7	25.3	–0.779	.996
	vs.	Crushed (18%)	–1914.7	28.2	–67.807	**< .001**
	vs.	Crushed (21%)	–743.0	25.3	–29.419	**< .001**
	vs.	Crushed (24%)	–240.7	25.3	–9.529	**< .001**
Rounded (24%)	vs.	Blended (18%)	–501.0	25.3	–19.837	**< .001**

	vs.	Blended (21%)	–115.3	25.3	–4.567	**.006**
	vs.	Blended (24%)	–36.7	25.3	–1.452	.862
	vs.	Crushed (18%)	–1931.7	28.2	–68.409	**< .001**
	vs.	Crushed (21%)	–760.0	25.3	–30.092	**< .001**
	vs.	Crushed (24%)	–257.7	25.3	–10.202	**< .001**
Blended Matrix (M)						
Blended (18%)	vs.	Blended (21%)	385.7	25.3	15.270	**< .001**
	vs.	Blended (24%)	464.3	25.3	18.385	**< .001**
	vs.	Crushed (18%)	–1430.7	28.2	–50.667	**< .001**
	vs.	Crushed (21%)	–259.0	25.3	–10.255	**< .001**
	vs.	Crushed (24%)	243.3	25.3	9.635	**< .001**
Blended (21%)	vs.	Blended (24%)	78.7	25.3	3.115	.108
	vs.	Crushed (18%)	–1816.3	28.2	–64.325	**< .001**
	vs.	Crushed (21%)	–644.7	25.3	–25.525	**< .001**
	vs.	Crushed (24%)	–142.3	25.3	–5.636	**< .001**
Blended (24%)	vs.	Crushed (18%)	–1895.0	28.2	–67.111	**< .001**
	vs.	Crushed (21%)	–723.3	25.3	–28.640	**< .001**

	vs.	Crushed (24%)	–221.0	25.3	–8.750	**< .001**
Crushed Matrix (C)						
Crushed (18%)	vs.	Crushed (21%)	1171.7	28.2	41.494	**< .001**
	vs.	Crushed (24%)	1674.0	28.2	59.284	**< .001**
Crushed (21%)	vs.	Crushed (24%)	502.3	25.3	19.890	**< .001**

B.3 Porosity

Table B.3.1 gives the full interaction matrix for all nine mix combinations for porosity.

Table B.3.1: Porosity Full Interaction Matrix (Aggregate × b/a)

Baseline Combination	**vs.**	**Comparison Combination**	**Mean Difference**	**Standard Error (SE)**	**t-statistic**	**pTukey**
Rounded Matrix (R)						
Rounded (18%)	vs.	Rounded (21%)	0.5833	0.288	2.022	.549
	vs.	Rounded (24%)	0.6400	0.288	2.219	.436
	vs.	Blended (18%)	0.1567	0.288	0.543	1.000
	vs.	Blended (21%)	0.2333	0.288	0.809	.995
	vs.	Blended (24%)	0.4133	0.288	1.433	.870
	vs.	Crushed (18%)	–0.1800	0.323	–0.558	1.000
	vs.	Crushed (21%)	0.9267	0.288	3.213	.090

	vs.	Crushed (24%)	0.6167	0.288	2.138	.482
Rounded (21%)	vs.	Rounded (24%)	0.0567	0.288	0.196	1.000
	vs.	Blended (18%)	–0.4267	0.288	–1.479	.850
	vs.	Blended (21%)	–0.3500	0.288	–1.213	.942
	vs.	Blended (24%)	–0.1700	0.288	–0.589	.999
	vs.	Crushed (18%)	–0.7633	0.323	–2.367	.359
	vs.	Crushed (21%)	0.3433	0.288	1.190	.948
	vs.	Crushed (24%)	0.0333	0.288	0.116	1.000
Rounded (24%)	vs.	Blended (18%)	–0.4833	0.288	–1.676	.753
	vs.	Blended (21%)	–0.4067	0.288	–1.410	.879
	vs.	Blended (24%)	–0.2267	0.288	–0.786	.996
	vs.	Crushed (18%)	–0.8200	0.323	–2.543	.279
	vs.	Crushed (21%)	0.2867	0.288	0.994	.981
	vs.	Crushed (24%)	–0.0233	0.288	–0.081	1.000
Blended Matrix (M)						
Blended (18%)	vs.	Blended (21%)	0.0767	0.288	0.266	1.000
	vs.	Blended (24%)	0.2567	0.288	0.890	.991

	vs.	Crushed (18%)	–0.3367	0.323	–1.044	.975
	vs.	Crushed (21%)	0.7700	0.288	2.669	.229
	vs.	Crushed (24%)	0.4600	0.288	1.595	.795
Blended (21%)	vs.	Blended (24%)	0.1800	0.288	0.624	.999
	vs.	Crushed (18%)	–0.4133	0.323	–1.282	.924
	vs.	Crushed (21%)	0.6933	0.288	2.404	.341
	vs.	Crushed (24%)	0.3833	0.288	1.329	.909
Blended (24%)	vs.	Crushed (18%)	–0.5933	0.323	–1.840	.658
	vs.	Crushed (21%)	0.5133	0.288	1.780	.694
	vs.	Crushed (24%)	0.2033	0.288	0.705	.998
Crushed Matrix (C)						
Crushed (18%)	vs.	Crushed (21%)	1.1067	0.323	3.432	.060
	vs.	Crushed (24%)	0.7967	0.323	2.470	.310
Crushed (21%)	vs.	Crushed (24%)	–0.3100	0.288	–1.075	.971

B.4 7-day Splitting Tensile Strength (ITS)

Table B.4.1 gives the full interaction matrix for all nine mix designs for splitting tensile strength.

Table B.4.1: Splitting Tensile Strength Full Interaction Matrix (Aggregate × b/a)

Baseline Combination	vs.	Comparison Combination	Mean Difference	Standard Error (SE)	t-statistic	pTukey
Rounded Matrix (R)						
Rounded (18%)	vs.	Rounded (21%)	0.05000	0.0767	0.652	.999
	vs.	Rounded (24%)	–0.25000	0.0767	–3.259	.083
	vs.	Blended (18%)	–0.25000	0.0767	–3.259	.083
	vs.	Blended (21%)	–0.25333	0.0767	–3.303	.077
	vs.	Blended (24%)	–0.51000	0.0767	–6.649	**< .001**
	vs.	Crushed (18%)	–0.51167	0.0858	–5.966	**< .001**
	vs.	Crushed (21%)	–0.58667	0.0767	–7.648	**< .001**
	vs.	Crushed (24%)	–0.36667	0.0767	–4.780	**.004**
Rounded (21%)	vs.	Rounded (24%)	–0.30000	0.0767	–3.911	**.024**
	vs.	Blended (18%)	–0.30000	0.0767	–3.911	**.024**
	vs.	Blended (21%)	–0.30333	0.0767	–3.954	**.022**
	vs.	Blended (24%)	–0.56000	0.0767	–7.300	**< .001**
	vs.	Crushed (18%)	–0.56167	0.0858	–6.549	**< .001**
	vs.	Crushed (21%)	–0.63667	0.0767	–8.300	**< .001**
	vs.	Crushed (24%)	–0.41667	0.0767	–5.432	**.001**

Rounded (24%)	vs.	Blended (18%)	1.11e-16	0.0767	1.45e-15	1.000
	vs.	Blended (21%)	–0.00333	0.0767	–0.0435	1.000
	vs.	Blended (24%)	–0.26000	0.0767	–3.389	.065
	vs.	Crushed (18%)	–0.26167	0.0858	–3.051	.121
	vs.	Crushed (21%)	–0.33667	0.0767	–4.389	**.009**
	vs.	Crushed (24%)	–0.11667	0.0767	–1.521	.831
Blended Matrix (M)						
Blended (18%)	vs.	Blended (21%)	–0.00333	0.0767	–0.0435	1.000
	vs.	Blended (24%)	–0.26000	0.0767	–3.389	.065
	vs.	Crushed (18%)	–0.26167	0.0858	–3.051	.121
	vs.	Crushed (21%)	–0.33667	0.0767	–4.389	**.009**
	vs.	Crushed (24%)	–0.11667	0.0767	–1.521	.831
Blended (21%)	vs.	Blended (24%)	–0.25667	0.0767	–3.346	.071
	vs.	Crushed (18%)	–0.25833	0.0858	–3.012	.129
	vs.	Crushed (21%)	–0.33333	0.0767	–4.345	.010
	vs.	Crushed (24%)	–0.11333	0.0767	–1.477	.851
Blended (24%)	vs.	Crushed (18%)	–0.00167	0.0858	–0.0194	1.000

	vs.	Crushed (21%)	–0.07667	0.0767	–0.999	.981
	vs.	Crushed (24%)	0.14333	0.0767	1.869	.641
Crushed Matrix (C)						
Crushed (18%)	vs.	Crushed (21%)	–0.07500	0.0858	–0.875	.992
	vs.	Crushed (24%)	0.14500	0.0858	1.691	.744
Crushed (21%)	vs.	Crushed (24%)	0.22000	0.0767	2.868	.166